INVESTIGATION OF POWER TURBINE CASING THERMAL ENVIRONMENT USING ONE DIMENSIONAL THERMAL-FLUID NETWORK SOLVER

by

Ömer Uyav

B.S., Mechanical Engineering, Kocaeli University, 2019

Submitted to Institute for Graduate Studies in
Science and Engineering in partial fulfillment of
the requirements for the degree of
Master of Science

Graduate Program in Mechanical Engineering
Boğaziçi University

2023

ACKNOWLEDGEMENTS

First of all, I would like to thank my thesis advisor Prof. Dr. Hasan Bedir for his continuous support during my study. His encouragement, patience, and immense knowledge allowed me to finish my research.

I would like to thank Tusas Engine Industry (TEI) and my collegues Dr. Erinç Erdem, Dr. Volkan Tatar, Ahmet Cihat Arıkan, Ahmet Yasin Sedef, Emre Egemen, Hakan Emiralioğlu, and Mutlu Elmas for their feedbacks while I was creating the model and writing the thesis.

I would like to thank James Bruns at Altair Engineering Inc. for his helps while I have encountered errors in the Flow Simulator.

I would like to thank Ahmet Yasin Karabay, Akın Çağlayan, Ertuğrul Altun, and İlke Barış Özsüt who are my friends, colleagues, and ex co-workers for their motivation and support while I was enrolling the Boğaziçi University as a Master Degree candidate.

My sincere thanks also go to my family: My parents Nurşen-Kamil and my brother Uğur Önder always supported me without any question.

Finally, I am a lucky person to have such a wife, Ayşenur, who always be with me. Throughout the master degree period, I would like to thank her for her patience, motivation, and encouragement.

ABSTRACT

INVESTIGATION OF POWER TURBINE CASING THERMAL ENVIRONMENT USING ONE DIMENSIONAL THERMAL-FLUID NETWORK SOLVER

The gas turbine engine operates in high-temperature, instantly changing power demand and various atmospheric conditions. Therefore, turbine inlet temperature and material selection are among the most critical parameters to maintain its integrity and satisfy power output. However, the higher the turbine inlet temperature is, the less operational time is. Thus, cooling the engine components is crucial regarding the durability, integrity, and reliability of both rotating and structural parts and for controlling blade tip clearances. In addition, thermal and secondary air systems design collectively play a key role in the successful case cooling, as they determine the heat load and cooling flow distribution. The first tool of engineers for an initial concept design is a 1D simulation to create a new cooling system. However, this step can be challenging for designers due to the absence of a 1D modeling methodology in the literature. Therefore, this paper aims to present a 1D network modeling methodology for any turbine geometry at the preliminary design stage. In this sense, a test campaign is carried out to obtain the temperature distribution of a generic power turbine casing using thermocouples and pressure sensors. In addition, a 1D thermo-fluid steady-state model is established. The results of the model are validated against test data. Additionally, a sensitivity analysis is performed, which helps to determine critical geometric locations for the base model and to measure how the model is affected by boundary conditions. Furthermore, another casing geometry with a different cooling system is designed to examine temperature distribution variation on the casing by changing the conduction path of components. Finally, comprehensive comparisons of the geometries with advantages and disadvantageous are considered, and the result of the sensitivity analysis is evaluated.

ÖZET

GÜÇ TÜRBİNİ MUHAFAZASININ TERMAL ORTAMININ BİR BOYUTLU TERMAL-AKIŞ AĞ ÇÖZÜCÜSÜ İLE İNCELENMESİ

Bir gaz türbinli motor, yüksek sıcaklıkta anında değişen güç talebine ve çeşitli atmosferik koşullarda çalışacak şekilde tasarlanır. Bu beklentiler göz önünde bulundurulduğunda türbin giriş sıcaklığı ve malzeme seçimi, motorun bütünlüğünü korumak ve istenilen gücü elde etmek için en kritik parametreler arasındadır. Ancak türbin giriş sıcaklığı ne kadar yüksek olursa motorun ömrü o kadar kısa olur. Bu nedenle motor bileşenlerinin soğutulması hem dönen hem de sabit parçalarının dayanıklılığı, bütünlüğü, güvenilirliği ve kanat ucu açıklıklarının kontrol edilmesi açısından çok önemlidir. Ek olarak, termal ve ikincil hava sistemi tasarımı ısı yükünü ve soğutma havası dağılımını belirledikleri için güç türbini muhafaza soğutmasında önemli bir rol oynar. Konsept tasarımı aşamasında yeni bir soğutma sistemi oluşturmak için mühendislerin ilk danıştığı araç bir boyutlu simülasyon programlarıdır. Ancak literatürde uygun bir boyutlu modelleme metodolojisinin bulunmaması nedeniyle bu adım tasarımcılar için zorlayıcı olabilir. Bu tez, ön tasarım aşamasındaki herhangi bir türbin muhafaza geometrisi için bir boyutlu ağ modelleme metodolojisi sunmayı amaçlamaktadır. Bu anlamda, sıcaklık ve basınç sensörleri kullanılarak bir güç türbini muhafazasının sıcaklık dağılımını elde etmek için bir test kampanyası yürütülmüştür. Kurulan bir boyutlu model, testin kararlı noktaya ulaştığı andaki sonuçlarına göre doğrulanmıştır. Ayrıca, bir boyutlu modelin kritik geometrik konumların belirlenmesine ve modelin sınır koşullarından nasıl etkilendiğinin ölçülmesine yardımcı olan bir hassasiyet analizi gerçekleştirilmiştir. Ek olarak, bileşenlerin iletim yollarını değiştirerek muhafaza üzerindeki sıcaklık dağılımının nasıl değiştiğini incelemek için farklı bir soğutma sistemine sahip yeni bir muhafaza geometrisi tasarlanmıştır. Son olarak, duyarlılık analizinin sonuçları değerlendirilmiştir ve önerilen geometrinin avantajları ve dezavantajları ele alınmıştır.

TABLE OF CONTENTS

LIST OF FIGURES

LIST OF TABLES

LIST OF SYSMBOLS

A	Area, [m²]
C_d	Discharge coefficient
c_p	Specific heat, [J/kgK]
d	Diameter, [m]
D_h	Hydraulic diameter, [m]
D_{h_eff}	Effective hydraulic diameter, [m]
f	Fanning friction factor
F	View factor
g	Acceleration of gravity, [m/s²]
h	Heat transfer coefficient, [W/m²K]
k	Thermal conductivity, [W/mK]
L	Length, [m]
l	Length, [m]
$\dot{m}$	Mass flow rate, [kg/s]
Ma	Mach Number
Nu	Nusselt number, $= {hL}/{k}$
P	Perimeter
P_{amb}	Ambient pressure, [kPa]
P_s	Static pressure, [kPa]
$P_{s,down}$	Static pressure of downstream flow, [Pa]
$P_{t,ups}$	Total pressure of upstream flow, [Pa]
Pr	Prandtl number, $= {\upsilon}/{\alpha}$

q	Heat flow, [W]
r	Radius, [m]
R	Specific gas constant, [J/molK]
Ra	Rayleigh number, $= {g\beta(T_{metal} - T_{amb})L^3}/{\upsilon\alpha}$
Re	Reynolds number, $= {\rho v L}/{\mu}$
Re_{rot}	Rotational Reynolds number
T	Temperature, [K or °C]
T_{air}	Total temperature of air, [K or °C]
T_{amb}	Ambient temperature, [K or °C]
T_{metal}	Metal surface temperature, [K or °C]
T_t	Total temperature, [K or °C]
$T_{t,rel}$	Relative total temperature, [K or °C]
$T_{t,ups}$	Total temperature of upstream flow, [K]
v	Velocity, [m/s]
V_t	Tangential velocity, [m/s]
XK	Swirl ratio
α	Thermal diffusivity, [m²/s]
β	Coefficient of thermal expansion, [1/K]
γ	Specific heat ratio
Γ_{rotor}	Rotor surface torque, [Nm]
Γ_{stator}	Stator surface torque, [Nm]
ε	Emissivity

η	Scaling factor
μ	Dynamic viscosity, [kg/ms]
ρ	Density, [kg/m³]
σ	Stefan-Boltzman coefficient
υ	Kinematic viscosity, [m²/s]
ω	Angular velocity, [rad/s]

LIST OF ACRONYMS / ABBREVATIONS

1D	One Dimensional
2D	Two Dimensional
3D	Three Dimensional
CFD	Compututional Fluid Dynamics
CHT	Conjugate Heat Transfer
FEM	Finite Element Method
FS	Flow Simulator
HTC	Heat Transfer Coefficient
MTO	Maximum Take-Off
OEM	Original Equipment Manufacturer
PT	Power Turbine
RANS	Reynolds Averaged Navier-Stokes
SAS	Secondary Air System

Subscripts

CCT	Coupling Correction Term
fluid	Fluid
HT	Heat Transfer
L	Left
lam	Laminar flow region
R	Right
film	Film

tran	Transition flow region
turb	Turbulent flow region

1. INTRODUCTION

Turbomachinery has a prominent role in aviation, defense, and power generation industries that require high technology and complex integration of multidisciplinary expertise. In order to improve the current technology to higher level, consolidation of the disciplines has been revolved around some rules throughout the history. One of the most distinguished rules is a thermodynamic cycle, called Brayton Cycle.

Brayton cycle is an open thermodynamic cycle that includes the main components of any turbomachine which are compressor, combustion chamber, and turbine. These components are mounted on the same shaft and constitute the whole cycle, shown in Figure 1.1.

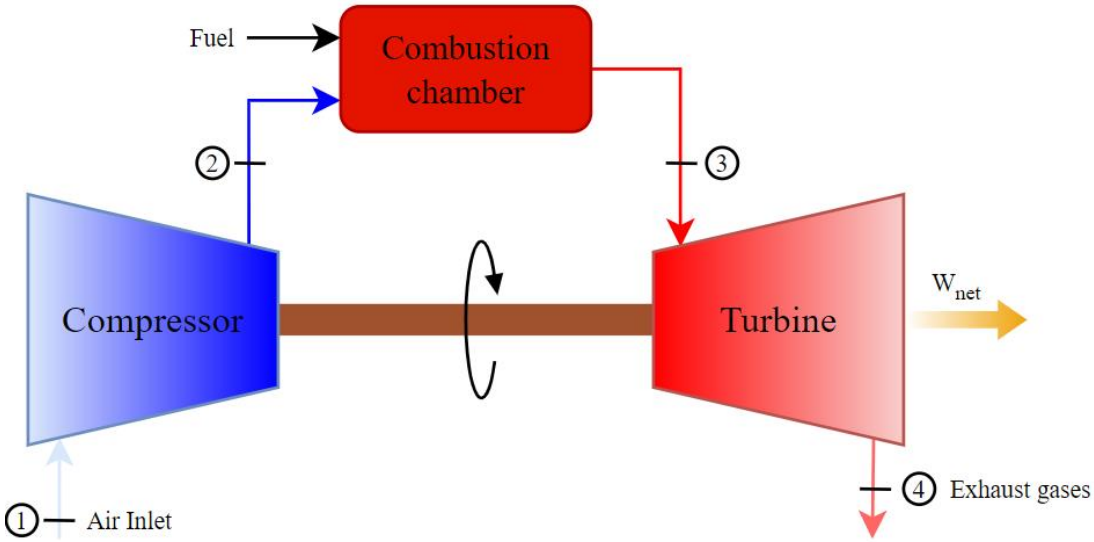

Figure 1.1. A schematic of an open Brayton cycle.

In the cycle, the fresh air, or ambient air, enters the compressor and the pressure of the air as well as temperature increases due to work done by the compressor from 1 to 2. The temperature of the compressed air is increased in the combustion chamber with additional fuel on the system (between 2 and 3). After here, the hot gas enters the turbine stage, and some part of the inherent energy of the air is converted to produce work output while other part is used to produce exhaust gases, in other word thrust (3-4).

The characteristic of the turbomachine is shaped by adding additional modules on the cycle according to the demands of the platforms. Namely, thrust and shaft output percentages can be controlled thanks to additional modules. Within the scope of the thesis, a turbomachine that require high work output instead of thrust is considered.

A power turbine (PT) is optimized to produce shaft power rather than jet thrust. In concept, a power turbine is an additional module to any gas turbine providing an extra expansion to extract heat energy from the exhaust and convert it into output shaft power. Power turbines are commonly used in applications that require a sustained high-power output, high reliability, small size, and lightweight. These include helicopters, auxiliary power units, tanks, ships, boats, hovercraft, and stationary equipment.

A power turbine engine may be made up of two significant parts; the 'gas generator' and the 'power generator.' The gas generator consists of the compressor, combustion chambers with igniters and fuel nozzles, and one or more turbine stages. The power generator consists of additional turbine stages, a gear reduction system, and the shaft output. The gas generator creates hot expanding gases to drive the power generator. Depending on the design, the engine accessories may be driven either by the gas generator or the power section. The sections constructing a power turbine are shown in Figure 1.2.

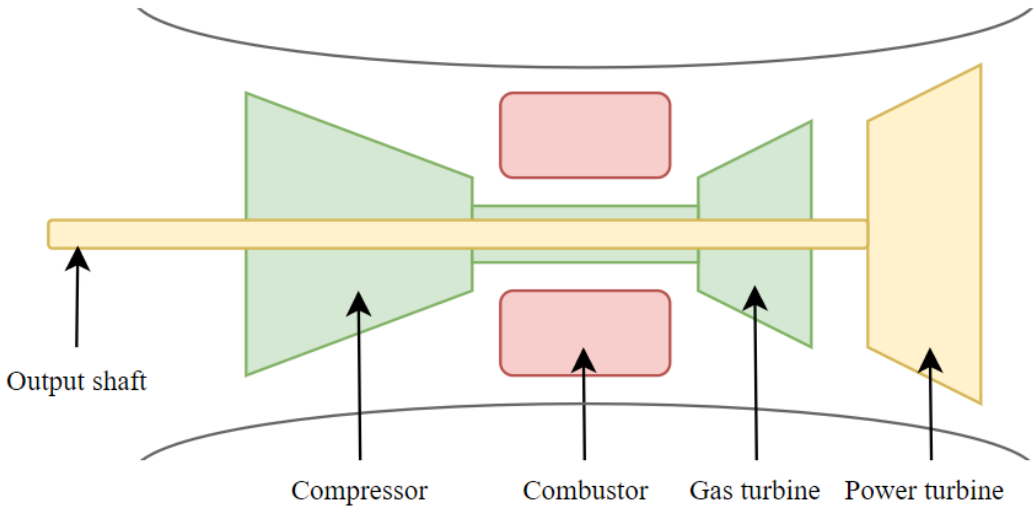

Figure 1.2. A schematic power turbine.

Air in the engine is separated two categories depending on its function: Primary flow and Secondary flow. The primary flow produces jet thrust or shaft power, and the secondary flow is used for other requirements.

The air extracted from the compressor stage for cooling components pressurized the internal region to balance engine aero and bearing loads, ensuring sealing between regions like rotor-stator cavities, clearance control, and ventilation of the sump region to avoid any fire risk is called secondary flows. The entire system driven by the secondary flows is known as Secondary Air System (SAS). In addition to these functions, the SAS flow can be used for customer services and anti-icing systems. This flow has no contribution to the thrust. Such air flows are fed from the compressor flow being relatively cold and high pressure. Then, it is distributed to the turbine SAS flow path as the sink. Throughout the path, the flow interacts with many components like labyrinth seals, rotor-stator cavities, orifices, and other types of restrictions [1].

The cooling of a PT Casing is an essential phenomenon for an engine in terms of durability, integrity, reliability, and blade tip clearance control. Therefore, thermal management and Secondary Air System design of the engine play a crucial role in the efficiency of the turbine. The uniform temperature distribution through the casing is provided with a carefully designed thermal and SAS environment.

Many OEMs widely accept the use of multi-dimensional computational software to design thermal and SAS networks because of their robustness and reliable outcomes. In addition, the software eliminates the necessity of experiments that are time-consuming and involves a fair amount of labor force. Modeling the system in a computer medium therefore is a convenient solution.

This thesis proposes a 1D thermo-fluid network methodology for thermal system designers at the preliminary design stage. Subsequently, the network results are compared with the engine test result carried out in a campaign. Moreover, a sensitivity analysis is performed to figure out the critical parameters affecting the thermal gradient on solid parts

and the internal pressure of the casing. Finally, a geometric improvement of the current geometry is offered to reduce the conduction effect between components and increase the cooling capability of the engine.

Chapter 2 consists of a literature review on one or more dimensional modeling of turbomachinery. Chapter 3 includes the objective of the thesis. Details of the test campaign is given in Chapter 4, followed by brief information about Flow Simulator and details of the modeling methodology in Chapter 5. The test and model results are compared in Chapter 6 including boundary condition and heat transfer coefficient values. In the same chapter, sensitivity analysis and geometric improvement are presented. Lastly, Chapters 7 comprises of Conclusion.

2. LITERATURE

The literature has had several studies which enlightened one and more dimensional modeling approaches in past years. In addition, the approaches have been enriched with coupling strategies, test campaigns, and computational methodologies. Package software programs have taken a crucial part in these studies while these works have been done.

Thorpe et al. [2] evaluated the impacts of rotor tip leakages on a transonic axial turbine casing, finding major factors affecting heat loads and heat transfer. The paper was constructed on an engine-representative experimental setup and supported by a time-based numerical model in order to clarify the aerothermal mechanism in the casing. The experimental results indicated that axial span between 35-60% at the rotor tip leakage is the dominant criterion affecting above 50% of casing heat transfer since the flow is stagnated in that span range. The temperature hence is increased.

Dann et al. [3] commissioned a new test facility to investigate the displacement of a high-pressure turbine casing under different external cooling conditions affecting rotor tip clearance. This facility also could evaluate different geometry to assess the cooling characteristic of the casing and control rotor tip clearances. The casing's displacement and temperatures were traced with sensors and thermocouples. An external heat source is used to simulate the actual engine temperature. At the end of the test, the test setup approached the engine operation temperature and showed that it could be allowed for the operation of different heat load conditions and case cooling being similar to engine level.

In another study, Dann et al. [4] created a full-scale test rig for a high-pressure turbine and compressor casing air system to figure out SAS flow impingement effects on the casing transient heat transfer mechanism. First, steady-state RANS analysis was run for two types of arrays to determine an efficient impingement array. Then, the 3D Unsteady Conjugate Heat Transfer model was analyzed for metal casing thermal distribution using

designed impingement arrays. Finally, the experimental results were compared with CFD regarding heat transfer coefficient.

Wang et al. [5] numerically investigated the temperature distribution of a combined cycle power plant's intermediate pressure turbine inner casing to find out the factors affecting the working life. The fluid side and heat transfer solutions were separately considered. The former side is that the 1D analytical method was used and the latter is that steady-state and transient solutions for the solid parts of the plant were calculated based on the results taken from the fluid side using 2D finite element method. Five different cap clearances between the outer and inner casing were altered from 0.01 mm to 0.5 mm to investigate temperature distribution. General assumptions were that the steam temperature was fixed, radiation was neglected, and conduction in steam was ignored. The study revealed that the leakage flow rate increased when the cap went up. The inner casing's average temperature reduced as the clearance decreased at the steady-state condition and thermal loads reached their maximum points at the transient condition. Then, the authors concluded that steam cooling was an effective solution to enhance the operational capability, increase durability and avoid thermal fatigue and creep.

Pilkington et al. [6] investigated the non-uniform cooling of the combustor casing when the engine was shut down. Because of the natural convection at the outer side, the inner side cools faster. Therefore, the cooling distorts the casing, affects blade tip clearance, and leads to rubbing. Due to these consequences, the dominant factor was the local temperature difference at the casing. Therefore, the author proposed two active natural convection controlling systems instead of a passive one (meaning baseline model): Purging air and air extraction. The former system did not eliminate the nonuniformity; however, the latter gave more uniform heat flux over the casing, decreasing the distortion. First, a transient CFD model for baseline geometry was established to achieve this conclusion, and the results were validated with test results. Then, CFD models for the proposed systems were conducted.

In another study, Muller [7] created a somewhat new SAS topology that directly integrates the 1D SAS network into the thermomechanical mesh setup. Thanks to this advanced approach, the author established a thermomechanical-fluid coupling process for a low-pressure turbine rotating at 14000 RPM using a commercial finite element software CalculiX and the new topology was also implemented to the CalculiX since it did not inherently possess this topology. An in-house program belonging to MTU Aero Engine, Flowmaster, was used to verify the new topology because the Flowmaster results had also been verified. Overall, the coupled model results calculated by CalculiX were well matched. The CalculiX results were also contrasted with the MTU SAS tool for mass flow rates, QTRAN for thermal, and ABAQUS for structural models while considered as a standalone model, and it confirmed once again that the topology appropriately worked with CalculiX.

In a similar study to the previous one, Tondello et al. [8] worked on a coupling process between SAS and the structural model to determine the temperature distribution of a gas turbine disk and labyrinth seal behavior throughout the operation envelope. This study was conducted on Flowmaster V7 for 1D SAS flow simulation and ANSYS for the 3D structural model at 22600 rpm nominal rotational speed. Flowmaster V7 inherently possesses a cavity solver using angular momentum conservation, torque balance, and swirl solver. Furthermore, the disk was divided into multiple solid domains, and each domain corresponded Flowmaster cavity. Hence, the parameters were linked between 1D and 3D models. Finally, the coupling process's convergence was viable, with less than 1% error.

Caty [9] created a FEM model that includes a thermal and SAS model for a triple-spool turbofan engine, to figure out how it reacts in different working conditions and the pros and cons of the two-spool engine configuration. While pre-processing, boundary conditions were taken from reliable performance cycle data, and the geometry was defined with engine representative inputs. During the analyses, PATRAN which is a commercial software for meshing and FLUID which is an in-house code owned by SNECMA for computation, were used. Afterward, various operating conditions such as take-off, cruise, deteriorated engine, and failure cases were also investigated to ensure the robustness and

reliability of the model. The results indicate that the created model can be adopted to further studies.

To decrease the computational time of the analyses, Alizadeh et al. [10] created a 1D model of turbine blades' internal cooling passages because the 3D model has a higher computational time. First, an in-house flow network solver was used to solve the complex internal blade geometry. An essential assumption was that the wall temperatures were selected as a fixed temperature, 850 K, for the sake of simplicity. Then, heat transfer and mass flow distribution were the model's outputs. Another aim of this study was to obtain the boundary condition of coolant for conjugate heat transfer analysis. However, there were no existing experimental literature data for similar cases for validation. Therefore, the constructed model was validated by using CFD results in the literature that are all validated. Furthermore, sensitivity analyses were carried out to determine the effect of coolant mass flow rate on wall temperature, inlet temperature, and corresponding efficiency variation. The result shows that the developed model was well enough when compared to referenced data, and also these results could be used for other typical blade geometries. In addition, coolant mass flows had less influence on wall and inlet temperature. Yet, coolant inlet temperature significantly affected efficiency, such that a 100 K increment in the temperature decreased 6.5% of convective efficiency.

Ganine et al. [11] studied on heterogeneous coupled model of a 1D SAS flow network in SPAN software using a quasi-steady approximation and unsteady thermo-mechanical 2D/3D model for engine parts in SC03. A 2D axisymmetric model of an intermediate-pressure turbine was used for analysis. The simulations were compared with intermediate pressure turbine experimental data on commercial turbofan engines and neglected coupling effects. The applied heterogeneous approach could predict mass flow rates, running clearances, temperatures, and pressures throughout the time-based operation envelope.

Ba et al. [12] conducted a coupled aero-thermal throughflow method regarding film cooling effects on blade temperature. The authors compared the method with the

experimental data of the NASA-C3X. The results showed that the comparison was agreed well, and the new method can be used to call for the blade wall temperature and determine the necessity of cooling flow budget at the preliminary design stage.

For the same engine component mentioned above in the previous study, Collins et al. [13] conducted a comprehensive film cooling study, including design, numerical modeling, and experimental test for an unshrouded high-pressure rotor casing. Because the casing is exposed to varied thermal load while working, adequate cooling of this region has a crucial impact on maintaining the engine's integrity, endurance, and performance. In this study, two different film cooling hole arrays, which differ in circumferential space, were carried out. First, an engine representative test campaign belonging to the Oxford Turbine Research Facility was used. Then, an uncertainty study for experimental results covering Nu and temperature variations was interpreted. For CFD analysis, 3D full-sector transient model was analyzed with ANSYS Fluent. In addition, the flow that passes through between the rotor tip and the casing was also evaluated concerning acoustic characteristics. At the end of the paper, the authors claimed that the simulation and experimental results are similar, film cooling could be an active solution for cooling the rotor under intermediate cooling mass flow rates condition, and the acoustic character of the tip region should be considered due to affect mass flux at the tip region.

Jalali et al. [14] generated a code that comprises 1D heat transfer predictions and fluid flow in turbine cooling passages. In code, 1D conservation equations, HTC correlations, and friction factor correlations were embedded. The solver result was validated with 3D CFD analysis and experimental data, and the 1D solver errors were less than 1.1% for pressure, temperature, and mass flow against CFD.

Hunt et al. [15] proposed a new approach called Implicit Conjugate Heat Transfer (CHT) to minimize simulation costs in analyzing the thermal fluid 1D coupled model. While the traditional explicit approach solves the 1D fluid model and uses the outputs as inputs for the 1D thermal model, or vice versa, and this iterative loop continues until it converges, the implicit approach provides functions for each element, which brings fast

convergence, high fidelity, and less computational work. In this study, the authors first tried this method on a simple duct flow and compared the results in the analytical model, 1D solid and 1D fluid CHT model, and 1D fluid 3D solid CHT model in Simcenter Flowmaster. The outcomes of these comparisons regarding solid and fluid temperatures were in good agreement. Afterward, this approach was imposed on a rotor-stator cavity. To demonstrate CHT model fidelity, they solved the cavity in two ways: Implicitly and explicitly. The results show that the implicit CHT model in Flowmaster converged more smoothly and rapidly than an explicit segmented model. In conclusion, the CHT approach provides high consistency and is helpful for preliminary design.

3. OBJECTIVE

3.1. Gaps in Literature

The current literature that is mentioned above section shows the last point that is reached relating to thesis scope. But even in these studies there are several gaps. Firstly, there are not any study that include PT casing 1D thermo-fluid network modeling. The closest study was conducted by Hunt et al. [15], who modeled Implicit CHT on a duct flow initially and then applied the modeling methodology to rotor-stator cavity. However, the study includes 3D model which is main difference comparing to the thesis. Secondly, most modeling strategy did not address any HTC correlation or any coefficient that suit for the 1D casing thermo-fluid modeling. Finally, some papers performed real engine or engine representative component tests by validating with one or more dimensional package software. The test in these studies was related to blade cooling mechanism and HPT or combustor casing.

To sum up, the gaps in the literature are briefly listed below:

- A 1D thermo-fluid network model of a PT Casing by calibrating with a real engine test
- Proper HTC correlation for a 1D PT Case model.

3.2. Thesis Objective

The first objective of this thesis is to create a 1D thermo-fluid network for a PT casing in the FS at the preliminary design stage and the FS model is calibrated with an engine test for an operation point. The following objective is to perform a sensitivity analysis for the parameters that affect heat transfer and fluid mechanism. These two directly fill the gaps that are mentioned above. The last objective is to propose a new modified casing geometry in order to control the metal temperatures of the casing components.

4. TEST DETAILS

To evaluate thermal and flow characteristic of the engine, a test campaign was conducted. The purpose of the test is to calibrate modeling methodologies being done at preliminary design stage and understand behavior of the engine while in operation envelope.

The whole module of the engine was entirely instrumented. Yet, PT Casing instrumentation layout was merely evaluated because of the scope of the thesis. Figure 4.1 shows instrumented PT Casing layout that totally consists of 72 parameters:

- 18 parameters for temperature of air.
- 30 parameters for metal surface temperature.
- 24 parameters for static pressure.

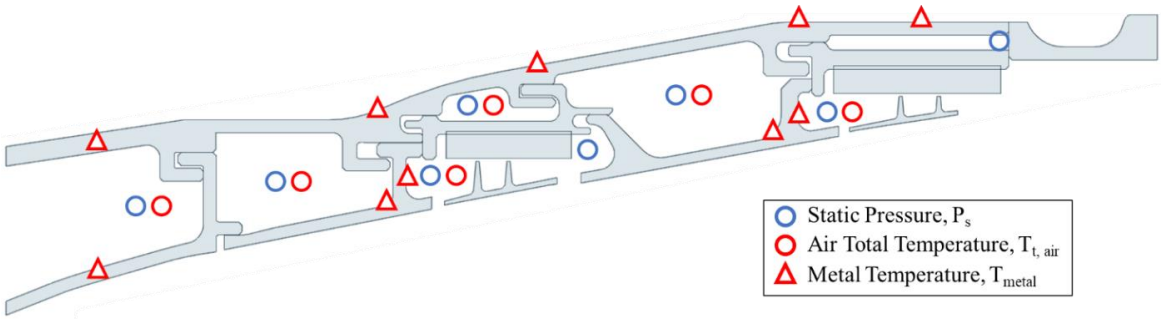

Figure 4.1. PT casing instrumentation layout.

Uncertainty of the sensors is the most crucial factor for measurement accuracy and the reliability of the test. Due to these matters of facts, the sensors and the thermocouples must be carefully selected. While selecting the proper instrumentation, working ranges of the engine in terms of temperature and pressure, routing applications of the sensors inside the engine, and environmental conditions must be also attentively designated. Considering all these conditions, Type K thermocouples were used for T_{metal} and T_t. The measurement range is 0 to 1260°C and the uncertainty is ±2.2°C or ±0.75%. For pressure sensor, the

measurement limit is varied depending on measurement location demand but uncertainty is ±0.05% for all of the pressure sensors.

Test cell ambient pressure and temperature are two of the most dominant parameters. The cell altitude above sea level must be carefully measured since it is assigned as inlet pressure of the engine, and the ambient temperature must be meticulously conditioned. Accordingly, T_{amb} is set to 288.15 K and P_{amb} is 92.5 kPa at the altitude where test campaign is mounted. In addition, the operation condition of the engine is Maximum Take-Off (MTO) which Re is 194330.

5. ONE DIMENSIONAL MODEL

Having discussed the experimental details, Flow Simulator theory, geometric details, modeling methodology, boundary conditions and finally model details will be discussed in the following sections.

A flow network is primarily constructed on two factors to increase the accuracy of results: First is conservation laws which are met for each junction and flow element in the network; second is empirical correlations based on real engine or engine representative test results and special test setups. But it should not be forgotten that the correlations need to be improved for newly designed or an existing element.

1D flow network modeling for each conduit is based on control volume analysis of mass, momentum, energy and entropy equations. For a compressible flow, the momentum equation couples with energy equation through density for the conduit, and the density is calculated using perfect gas equation. The most common flow elements that follow this modeling concept are pipe and orifice.

To initiate with a pipe element, the density, velocity and area in axial direction can be vary from inlet to outlet. Besides, it can be divided into multiple control volume that decreases error and increases precision of the calculation. For a steady-state condition, the mass flow yields in terms of Ma number as

$$\dot{m} = \frac{P_{t,ups} A C_d}{\sqrt{T_{t,ups}}} \sqrt{\frac{\gamma}{R}} \frac{Ma}{\left(1 + \frac{\gamma - 1}{2} Ma^2\right)^{\gamma+1/2(\gamma-1)}}, \tag{5.1}$$

or it can be written in terms of pressure as

$$\dot{m} = \frac{P_{t,ups} A C_d}{\sqrt{T_{t,ups}}} \sqrt{\frac{\gamma}{R}} \sqrt{\left(\frac{2}{\gamma - 1}\right)\left(\frac{P_{t,ups}}{P_{s,down}}\right)^{-\frac{\gamma+1}{\gamma}}\left[\left(\frac{P_{t,ups}}{P_{s,down}}\right)^{\frac{\gamma-1}{\gamma}} - 1\right]}, \tag{5.2}$$

where $\dot{m}$ is mass flow rate, $T_{t,ups}$ is upstream total temperature, $P_{t,ups}$ is upstream total pressure, A is area, C_d is discharge coefficient, γ is specific heat ratio, R is specific gas constant, Ma is Mach number, $P_{s,down}$ is downstream static pressure.

Pressure, shear and rotational body forces acting on the pipe control volume is considered while conserving linear momentum, and the steady flow linear momentum is given as

$$F_{pressure} - F_{shear} + F_{rotational} = \dot{m}(v_2 - v_1),$$

$$F_{pressure} = (P_{s,2} - P_{s,1})\frac{A_1 + A_2}{2},$$

$$F_{shear} = \left(\frac{A_1 + A_2}{2}\right)\left(\frac{f_1 + f_2}{2}\right)\left(\frac{v_1 + v_2}{2}\right)\left(\frac{\rho_1 + \rho_2}{2}\right)\frac{\Delta x}{2D_h}, \tag{5.3}$$

$$F_{rotational} = \left(\frac{A_1 + A_2}{2}\right)\left(\frac{\rho_1 + \rho_2}{2}\right)\omega^2\left(\frac{r_2^2 - r_1^2}{2}\right),$$

where $\dot{m}$ is mass flow rate, v is velocity, P_s is static pressure, A is area, ρ is density, f is Darcy friction factor, Δx is axial distance between inlet and outlet, D_h is hydraulic diameter, ω is angular velocity, r is radius, and subscripts 1 and 2 denote inlet and outlet, respectively.

The conservation of energy in the steady pipe flow consists of heat transfer at the wall and work transfer due to rotation, and the relative total temperature can be computed as

$$T_{t,rel_2} = T_{t,rel_1} + \left(\Delta T_{t,rel}\right)_{rotation} + \left(\Delta T_{t,rel}\right)_{HT} + \left(\Delta T_{t,rel}\right)_{CCT}. \tag{5.4}$$

The first term in the equation is inlet relative total temperature, the second term is change in temperature due to rotation which is formulated as

$$\left(\Delta T_{t,rel}\right)_{rotation} = \omega^2\left(\frac{r_2^2 - r_1^2}{2c_p}\right), \tag{5.5}$$

where ω is angular velocity, r is radius and c_p is specific heat, and subscripts 1 and 2 denote inlet and outlet, respectively.

The third term is change in temperature due to heat transfer and calculated, shown as

$$\left(\Delta T_{t,rel}\right)_{HT} = \left(T_w - T_{t,rel_1}\right)1 - e^{-\eta}\ ;\ \eta = \frac{hA}{\dot{m}c_p}, \tag{5.6}$$

where T_w is wall temperature, $T_{t,rel}$ is total relative temperature, $\dot{m}$ is mass flow rate, c_p is specific heat, A is cross-section area and h is heat transfer coefficient.

The last term is rotational work transfer and heat transfer coupling correction term derived by Sultanian [1] and it is computed as, shown as

$$\left(\Delta T_{t,rel}\right)_{CCT} = -\omega^2 r_1 \eta \left(\frac{r_2 - r_1}{2c_p}\right), \tag{5.7}$$

where ω is angular velocity, r is radius and c_p is specific heat, and subscripts 1 and 2 denote inlet and outlet, respectively.

Orifice element is the most ubiquitous element for 1D modeling [1]. It is able to use for restriction or metering the flow in stationary or rotating components. In concept, orifice element can also be presented as a short pipe. However, discharge coefficient calculation in the pipe element is not as advanced as orifice element. This is the most outstanding difference between a pipe and an orifice. While calculating proper C_d, the effects such as corner type (filler or chamfer), incidence angle, rotation, Re, and L/d ratio are considered.

Any flow element in the network requires upstream and downstream chambers (or node), placed between two chambers. These two chambers are a must for network modeling since flow element takes state variables from them. Due to this requirement, there are two types of junctions in a flow network model: Internal junction and Boundary junction.

The internal junction is able to connect with one or more flow element. Any internal junction (i) in a network has to conserve continuity equation and the continuity equaiton is written as

$$\sum_{i=1}^{n} \dot{m}_i = 0. \tag{5.8}$$

To ensure energy equation, the following equaiton should be met to compute mean outflow total temperature as

$$T_{t,mean\ outflow} = \frac{\sum_{i=1}^{n}\left(\dot{m}_1 T_{t,1} + \dot{m}_2 T_{t,2} + \cdots + \dot{m}_n T_{t,n}\right)_{inflow}}{\sum_{i=1}^{n}(\dot{m}_1 + \dot{m}_2 + \cdots + \dot{m}_n)_{outflow}}. \tag{5.9}$$

Any 1D network model has to at least one source and one sink, and a boundary junction is specialized for this purpose. The state variables that are defined in this junction are fix. Hence, whole model solution is based on the boundary junction.

5.1. Brief Flow Simulator Theory

Altair Flow Simulator (FS) is an integrated 1D heat transfer, flow, and combustion design software that enables network-based preliminary plus detailed design and analysis for any thermo-fluid system design applications. The software can analyze steady-state and transient models [16,17]. In addition, the FS network model can be modeled as coupled or standalone. The FS presents extensive flow and thermal element library for users to establish a model.

5.1.1. Flow Network Theory

In the FS, a flow network must include two building blocks which are flow chambers and flow elements. The chambers characterize the boundaries of the model having fixed

thermodynamics and fluid properties. Three distinct chamber types are commonly used in the FS:

- The plenum chamber that dissipates total quantities of entering flow by neglecting dynamic head to zero.
- The momentum chamber that calculates dynamic terms including incoming flow direction and then, it gives a vector direction to transfer the dynamic head through the downstream.
- The inertial chamber acting as momentum chamber except that it calculates fluid properties in stationary frame and transfers to rotating frame.

A chamber is an intersection point of the flow coming and leaving from an element. Then, the chambers solve continuity equation and those do not permit the accumulation of the fluid in the chamber. The continuity equation is expressed as

$$\sum Flow\ Entering = \sum Flow\ leaving. \tag{5.10}$$

Each chamber needs some certain flow inputs by users depending on its type and the users must enter these properties. Static pressure and total temperature are two main inputs for all chambers. Also, user can define swirl ratio as fixed or initial value.

A flow element calculates mass flow rate, exit flow state and element derivatives between an upstream chamber and a downstream pressure by using empirical correlations and formulations. In the element library, the FS consists plenty of element options to properly resemble flow physics such that tube, orifice types, and seal types are the most common element while modeling a network.

The orifice element contains different subtype orifices, and the Advanced Orifice is one of these types. In this thesis, the Advanced Orifice element is the only flow conduit in

the model since it acts like a combination of tube one orifice element. The theory of Advanced Orifice therefore is followingly mentioned.

The most distinctive feature of the Advanced Orifice is that the users can divide the orifice into multiple stations and circumferential segments. Thus, these divisions give flexibility to the users whilst modeling segment-by-segment heat transfer phenomena. The Advanced Orifice needs inputs by users. The cross-section shape, length, diameter, and wetted perimeter are the default mandatory requirements to solve the model.

The FS iteratively solves any model. Boundary chamber pressure is used as initial value and then, mass flow rate is calculated for each flow conduit. If the mass flow derivation with respect to pressure does not converge, the chamber pressure is adjusted until the derivation is converged.

The flow chart shown in Figure 5.1 gives basic procedure of solver methodology.

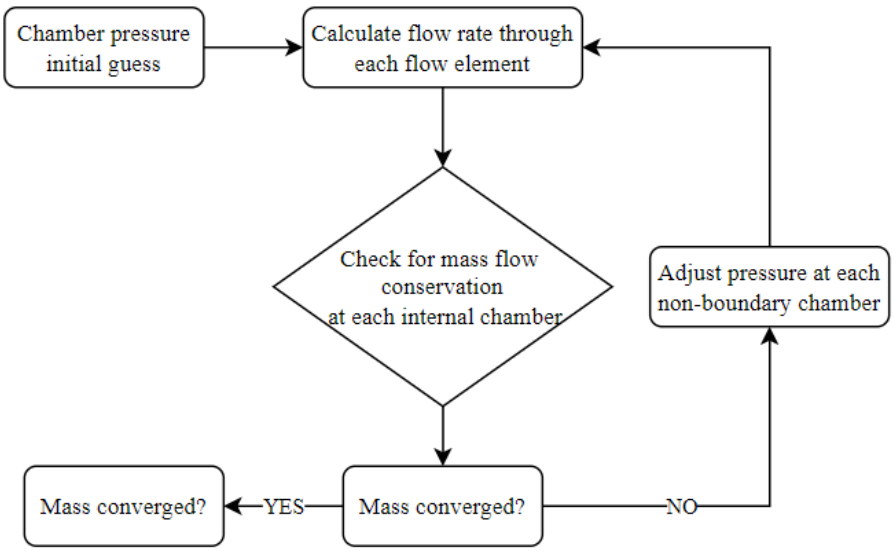

Figure 5.1. The FS simulation flow chart.

5.1.2. Thermal Network Theory

Another capability of the FS is thermal modeling. The users can easily integrate heat transfer to such model whether solve thermal model as standalone or couple with flow network and obtain combined results. Thermal network building block comprises two main features which are Thermal Nodes and Thermal Resistances.

There are two different thermal nodes in the FS: Boundary Thermal Node is a boundary node having a constant temperature value and Internal Temperature Node uses energy conservation equation to calculate the temperature where the heat coming from branches. Energy balance of the nodes is written as

$$\sum q_{L,R} = 0, \tag{5.11}$$

where subscripts L and R denote left and right thermal nodes, respectively.

Thermal resistance methodology constitutes building block of the FS thermal modeling. Each phenomenon being conduction, convection and radiation uses well known resistance equations. For conduction resistance, simple and radial resistance options are available to calculate heat flow rate depending on geometry, given as

Simple resistance: $$q_{L,R} = \frac{kA}{x}(T_L - T_R), \tag{5.12}$$

Radial resistance: $$q_{L,R} = \frac{2\pi Lk}{\ln\left({}^{r_2}/_{r_1}\right)}(T_L - T_R), \tag{5.13}$$

where k is thermal conductivity, A is cross-section area, x is distance between the nodes, T is temperature, L is length, r_2 is outer radius, and r_1 is inner radius.

The following equation shows convective resistance formulation used by the FS and it is expressed as

$$q_{L,R} = hA(T_L - T_R), \tag{5.14}$$

where h is heat transfer coefficient, A is surface area, T is temperature and subscripts L and R denote left and right temperatures.

If the convector is attached to a fluid chamber rather than any thermal node, the convector uses relative total temperature instead of absolute total temperature [16]. Therefore, rotation effect on temperature of the chamber can be taken into account accompanied by Swirl Ratio (XK). The swirl ratio is defined as the ratio of local tangential velocity and absolute tangential velocity, shown as

$$XK = \frac{V_t}{\omega r}, \tag{5.15}$$

where V_t is tangential velocity, ω is angular velocity and r is radius.

If XK is zero, absolute velocity equals to relative velocity since the system does not include any rotating components, and hence absolute total temperature and relative total temperature are equivalent to each other.

While calculating radiative heat transfer, Simple Radiator and Two Surface Radiator are used as

Simple Radiator: $$q_{L,R} = \sigma\varepsilon \mathrm{A}(T_L^4 - T_R^4), \tag{5.16}$$

Two Surface Radiator: $$q_{L,R} = \frac{\sigma(T_L^4 - T_R^4)}{\frac{1-\varepsilon_L}{\varepsilon_L \mathrm{A}_L} + \frac{1}{\mathrm{F}_{LR}\mathrm{A}_L} + \frac{1-\varepsilon_R}{\varepsilon_R \mathrm{A}_R}}, \tag{5.17}$$

where σ is Stefan-Boltzmann constant, ε is emissivity, F is view factor, A is surface area, and L and R subscripts denote left and right.

To solve Thermal Network, Newton`s method is employed to seek zero energy imbalance at node i, and it is formulated as

$$(\Delta q_{imb})_i = 0. \tag{5.18}$$

Then, Newton`s method is iteratively carried out by using Jacobian matrix in which heat resistors are formed as

$$\Delta q_{imb}^{n+1} = \Delta q_{imb}^{n} + \left(\frac{\partial q_{imb}}{\partial T}\right)\Delta T. \tag{5.19}$$

The FS inherently includes heat transfer coefficient correlations that are commonly known from the literature for forced and free convection conditions.

5.2. Geometry

The OEMs use different types of casings which serve the engine functionality. Therefore, each engine has unique structure. In this thesis, two stage power turbine casing including two pair of rotor-stator is examined. After here, Stator-1 (S1) and Rotor-1 (R1) represent first pair of rotor-stator and Stator-2 (S2) and Rotor-2 (R2) represent second pair of rotor-stator. The casing cross-section geometry is depicted in Figure 5.2. The figure also shows station locations with their numbers and labels.

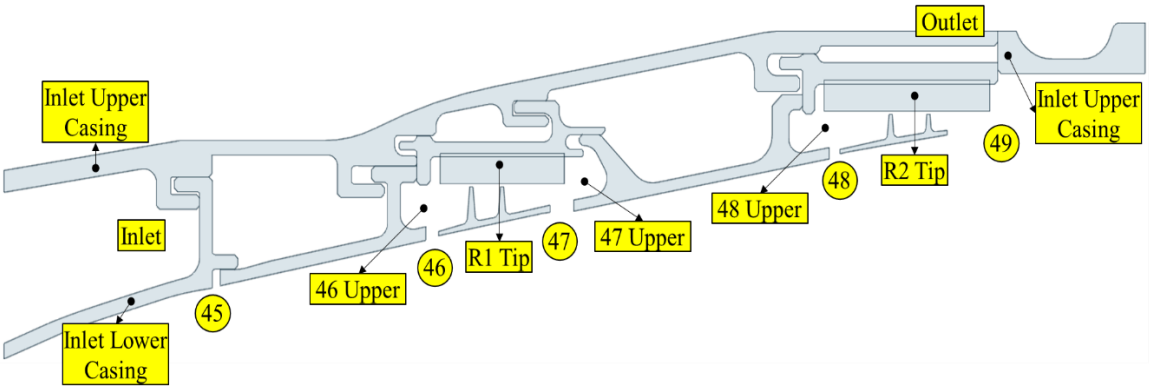

Figure 5.2. PT casing cross-section including station numbers and labels.

Material selection in the geometry is based on temperature which components face with. Due to this selection method, the casing and rotor-stator pairs are made from nickel based alloys.

5.3. Network Modeling

Within the scope of this study, 1D network modeling approach is applied to the geometry. While modeling, flow network is firstly structured. Then, thermal network is implemented onto the flow network. The reason of separate modeling is to simply determine proper flow chamber and elements for the geometry, and mitigate divergence problem.

5.3.1. Flow Network Modeling

As an initial step, cavities in the geometry are specified. Secondly, types of the cavities are assigned whether it is boundary or internal, or momentum chamber. Subsequently, dynamic head of the entering flow into a cavity should be evaluated with respect to lose it or not. Finally, the flow chamber which suits flow physic in the cavity is selected, mentioned in Section 5.1.1.

With this identification strategy, the attached flow chambers in the casing geometry are presented in Figure 5.3. While the yellow represents boundary chambers, the grey defines internal chambers.

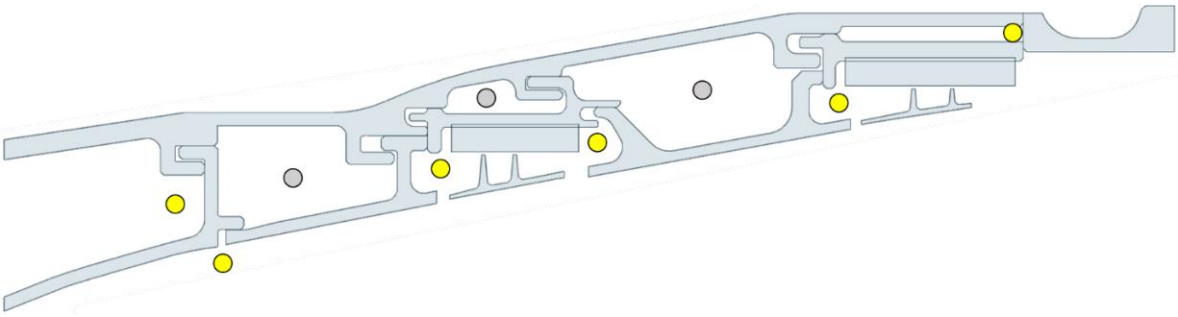

Figure 5.3. The FS flow chamber locations.

Following that flow elements are imported to the network model. In here, there is a limitation by FS which is that only Advanced Orifice and Tube Element are allowed

coupling process with thermal network. Thus, Advanced Orifice is selected as flow element for entire model. The main reason is that the Advanced Orifice is simpler than the Tube element meaning that the elapsed time whilst analyzing of the former is less than the latter. As thinking the complexity of the model, the simple flow element chose is much more convenient.

Advanced Orifice element has various cross-section shape option based on modeling geometry. The reason of multiple cross-section selection is to calculate Effective Hydraulic Diameter (D_{h_eff}). In the FS, mass flow rate is calculated depending upon D_{h_eff} which their formulation is described in Table 5.1 [18,19].

Table 5.1. Effective hydraulic diameter equation with aspect ratio [18,19].

Shape	**Effective Dh Equation**	**Aspect Ratio (AR)**
Circle	$\frac{Dh_{eff}}{Dh} = 1$	1
Rectangle	$\frac{Dh_{eff}}{Dh} = \frac{2}{3} + \frac{11}{24} * AR * (2 - AR)$	$\frac{r_2}{r_1}$
Ellipse	$\frac{Dh_{eff}}{Dh} = 1 - 0.2109 * (1 - AR)^2$	$\sqrt{\frac{\mathrm{P}^2 - \sqrt{(\mathrm{P}^4 - 6 * \pi^2 * \mathrm{A}^2)}}{\mathrm{P}^2 + \sqrt{(\mathrm{P}^4 - 16 * \pi^2 * \mathrm{A}^2)}}}$
Isosceles Triangle	$\frac{Dh_{eff}}{Dh} = \frac{64}{48 + 11.442 * AR - 6.0026 * AR^2}$	$\frac{1}{\left[2.19 * \left(\frac{\mathrm{P}^2}{\mathrm{A}}\right)^{1/3} - 4.83\right]^{1.5}}$
Annulus	$\frac{Dh_{eff}}{Dh} = \frac{1 + AR^2 + \frac{(1 - AR^2)}{ln\,(AR)}}{(1 - AR)^2}$	$\frac{r_2}{r_1}$
Arbitrary Shape	$\frac{Dh_{eff}}{Dh} = \frac{\sqrt{AR} * (1 + AR) * \left(1 - \left(\frac{192}{\pi^5}\right) * AR * tanh\left(\frac{\pi}{2 * AR}\right)\right)}{0.75 * \frac{Dh}{\sqrt{Area}}}$	$\frac{P - \sqrt{P^2 - 16 * A}}{P + \sqrt{P^2 - 16 * A}}$

As is known to all, gas turbine engine simply resembles annular geometry. Therefore, “Annular Cross-Section Shape” option is selected as shown in Figure 5.4. Then, area, perimeter, length, element orientation, and element multiplicity are defined.

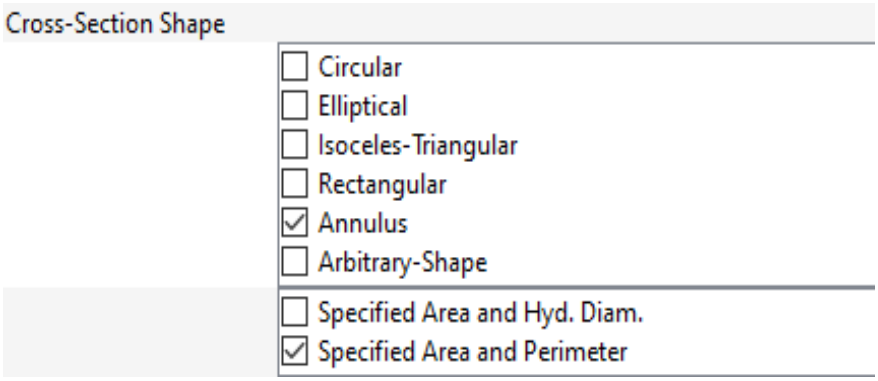

Figure 5.4. The FS cross-section shape selection.

5.3.2. Thermal Network Modeling

To couple thermal network with the flow network, proper association between them plays a crucial role by FS which should comply fundamental thermal resistance approach. The flow in the gas turbines looks like a duct flow. Thermal network thus follows duct flow modeling methodology because of this resemblance.

While modeling such a duct flow, FS has its methodology. A basic duct flow contains a flow region, inner and outer surfaces, and an ambient region. The cross-section of the duct perpendicular to the flow is depicted, and the corresponding thermal model in FS with element names is shown in Figure 5.5.

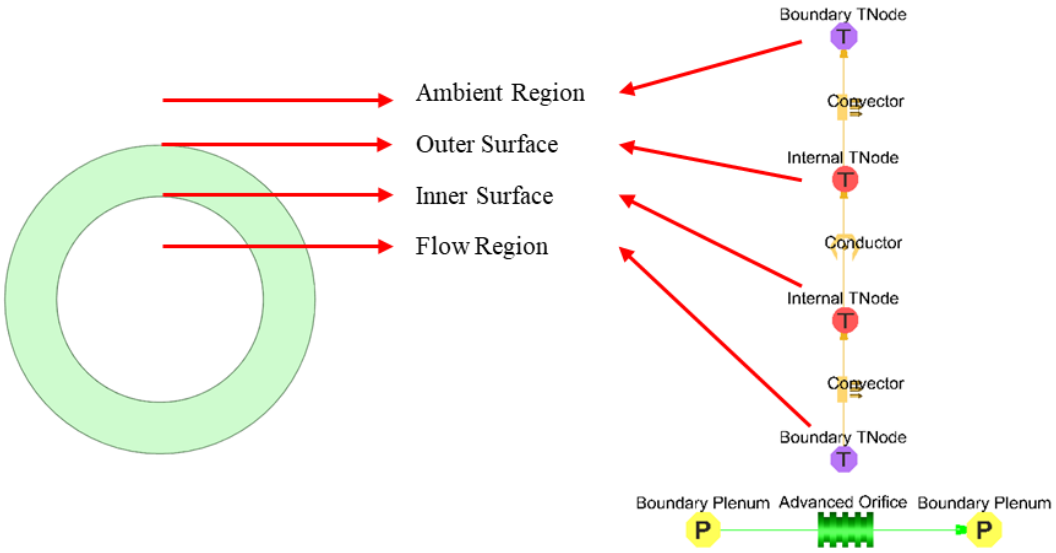

Figure 5.5. Thermal model of a duct flow in the FS.

The existing method in the FS is not adequate to model the geometry because a generic gas turbine engine geometry contains two annular sections instead of one. Due to this reason, a new annular flow modeling methodology in the FS must be established. Before describing the new technic, Figure 5.6 depicts how an annular cross-section of gas turbine casing is identified with section names.

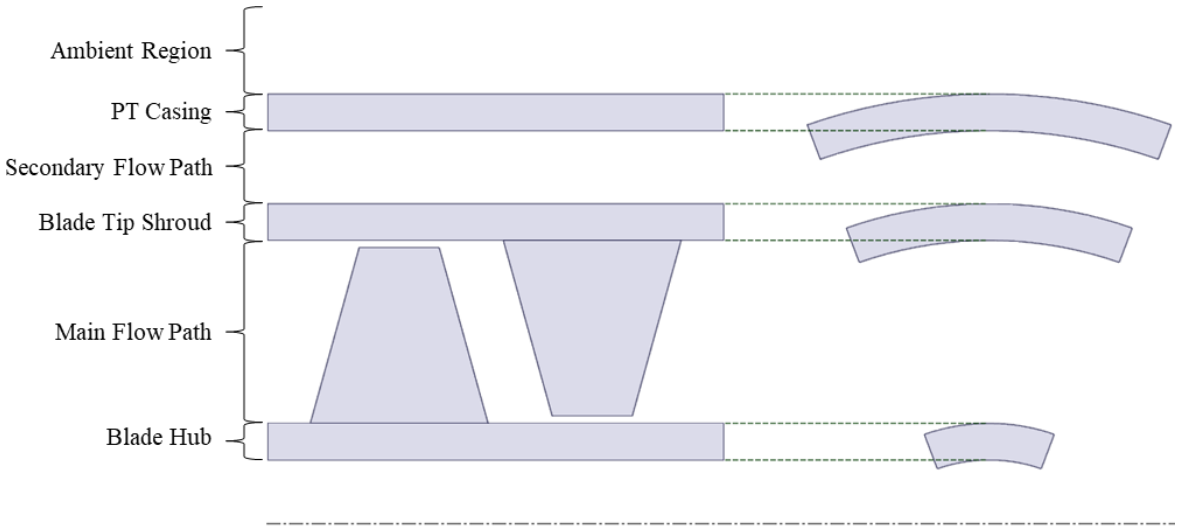

Figure 5.6. Section names of an annular cross-section.

In this thesis, the blade hub thermal effect is excluded from the model. Each thermal network located at the lower and upper sides of the Advanced Orifice element demonstrates thermal effects coming from the main flow path and how it affects the casing, shown in Figure 5.7.

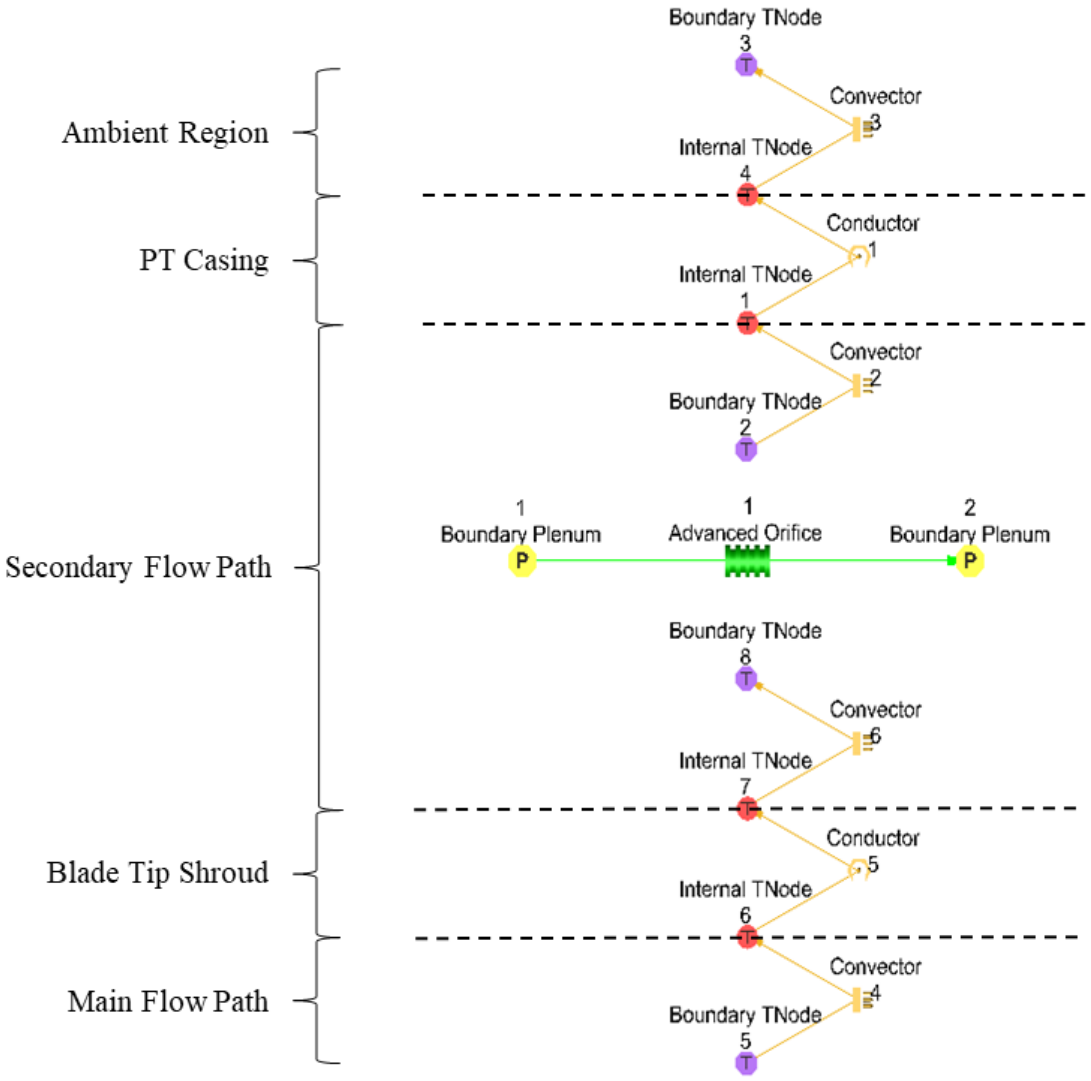

Figure 5.7. The advanced orifice thermal network modeling.

In the figure, Boundary TNode (BTN) 3 and 5 are boundary conditions in the model; the first is ambient temperature, and the second is main flow path temperature. BTN 2 and 8 state the same point, which denotes flow temperature in Advanced Orifice 1, but they are not boundary condition that is changing by the flow. Internal TNode (ITN) 1 and 4

represent the inner and outer surfaces of PT Casing, while ITN 7 and 6 represent the outer and inner surfaces of Blade Tip Shroud. Regarding thermal resistance, Conductors 1 and 5 define conductive heat transfer in solid parts. Convector (CONV) 3 represents natural convection heat transfer from the PT Casing outer surface to the ambient. CONV 4 defines the primary flow path convection, a calculated boundary condition from forced convection correlations in the literature. CONV 2 and 6 define convective heat transfer in the Secondary Flow Path from PT Casing Inner and Blade Tip Shroud Outer Surfaces.

In the FS, temperature-based properties are calculated from the temperature of flow element which is BTN 2 and 8 while pressure-based properties are computed from the upstream pressure of the flow element. The sources of non-dimensional numbers such as Nu, Re, and Pr rely on the properties and their references.

The basis of the study is established by using the methods cited above. In the following sections, the boundary conditions of the model will be explained first and then the model details will be given.

5.4. Boundary Conditions

In order to set boundary conditions of the FS model, some acceptations and assumptions are taken into account before obtaining them. One the most prominent acceptations is to use test result as boundary condition due to the fact that a certain part of the engine is examined in this study. Furthermore, the measurement cannot be taken at each station during the test. At some locations in the model, the test data are directly used as boundary condition while others are taken from CFD analysis.

Figure 5.8 shows which measurement locations in the test are used as boundary condition in the FS. Blue and red circles represent static pressure and total temperature boundary conditions taken by test result.

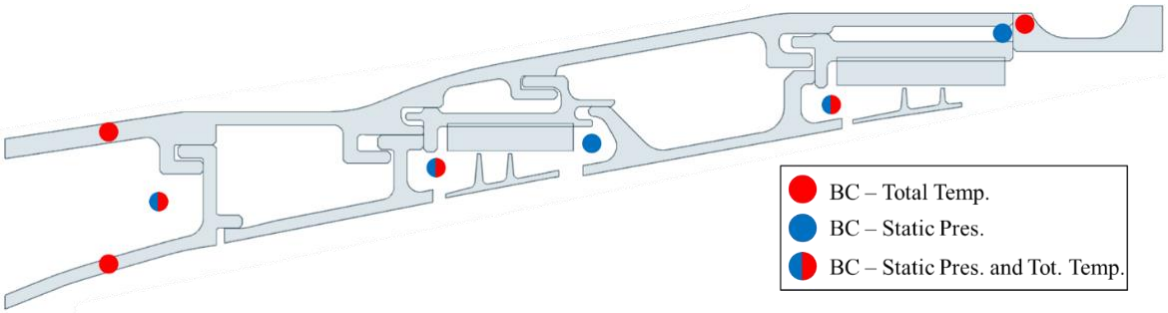

Figure 5.8. Boundary condition locations taken from the test.

According to post-test performance data of the engine which is a revised data of pre-test performance data based on the test results, a CFD analysis for the engine is carried out. However, since CFD analysis is not included within the scope of this thesis, it is merely continued with the results of it. The boundary condition value, P_s and T_t, for the rest of the stations are taken from the CFD. Figure 5.9 shows the locations where CFD results is used as inputs with same color notations in Figure 5.8.

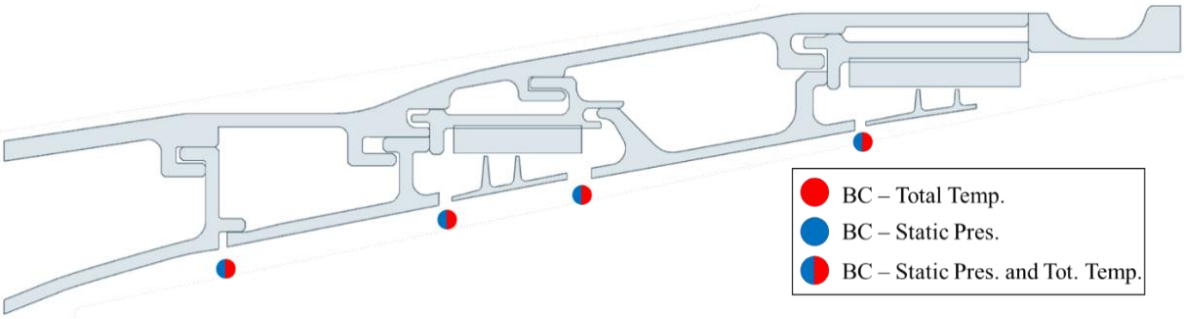

Figure 5.9. Boundary conditions taken from the CFD results.

Even then, there are just three locations remained which are R1_Tip, R2_Tip and 47_Upper. It is also mentioned that there is not any measurement neither the tips nor the 47_Upper. Therefore, a different method is followed, called Scaling Method.

Scaling method is a formulation to obtain a scaling factor to calculate unknown station values by using known station values. The known values act like a source and a sink. Then, scaling factor for unknown station is calculated and the formulation is shown as

$$\eta_{unknown} = \frac{T_{unknown} - T_{sink}}{T_{source} - T_{sink}}, \quad (5.20)$$

where η is scaling factor, and T is total temperature.

The most significant assumption in this study due to lack of test data in some stations is that pre-test scaling factor is used to calculate unknown station values in the FS because all station values in the pre-test data are known. Firstly, by utilizing the Equation 5.20, pre-test scaling factor are found for the remained three stations. In this step, 47_Upper is initially considered, and 46_Upper and 47 are chosen source and sink, respectively. Then, 46_Upper and 47_Upper for R1_Tip, and 48_Upper and 49 for R2_Tip is used as source and sink respectively. As a conclusion, η for the three unknown stations are calculated based on pre-test data.

To impart these scaling factors on the FS, the three unknown values for the FS model are calculated using the equation below obtained by manipulating Equation 5.20 that follows the same order in pre-test scaling factor. It should also be emphasized that the source and sink values mentioned in the equation are the boundary conditions that have been described so far and the input has been defined in the FS as

$$(T_{unknown})_{FS} = (T_{known})_{FS} + (\eta_{unknown})_{pre-test}(T_{source} - T_{sink})_{FS}, \quad (5.21)$$

where T is total temperature and η is scaling factor.

In summary, where the boundary conditions are taken from and how the unknown boundary conditions are calculated are mentioned in this section.

5.5. Modeling Details

The geometry is divided into four sectors that contribute to conveniently create thermo-fluid network in order to easily distinguish and to detect the errors. Also, this increases the control of the model by users. Figure 5.10 demonstrates the sectors with their names.

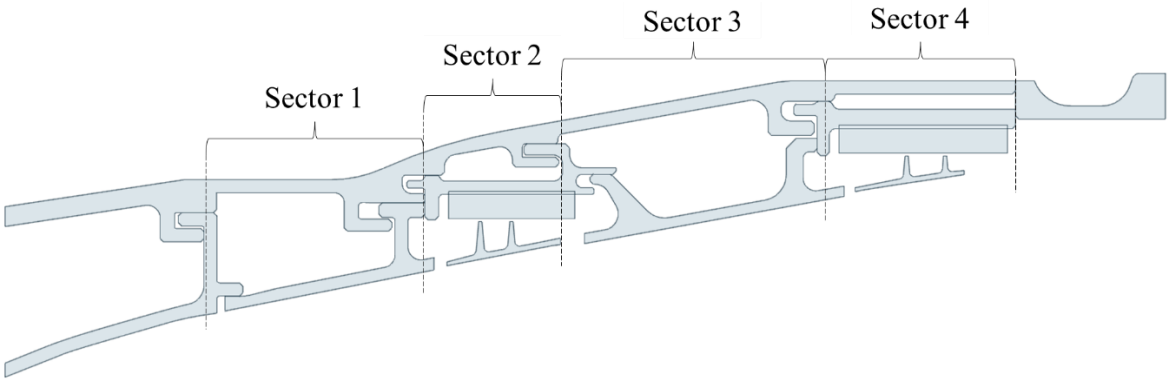

Figure 5.10. PT Casing sector names and locations.

While creating the network model, a basic strategy is followed: Boundary conditions of the Sector 1 is initially set, followed by flow and thermal network creation by using proper elements. Afterwards, geometric properties and HTC are defined. Lastly, the sector is fully analyzed. If the sector is converged, same procedure is applied for rest of the model.

5.5.1. HTC Selection

There are different heat transfer coefficient correlations which have particular characteristic depending on such as Reynolds number, Prandtl number, flow medium such as internal or external flow, and friction coefficient in open literature. Each coefficient has to be carefully selected so as to represent thermal effects on the model.

The FS incorporates some well-known heat transfer coefficient correlations in convector element. These correlations are able to serve variety of thermal modeling strategy. While modeling, friction is ignored in the entire model since dynamic head is lost and the cavities are large enough in the casing. Therefore, the HTC correlations belonging to Gnielinski [20] and Bhatti-Shah [21] include friction term, and the results are zero. As a conclusion, these two are not suitable for the model. According to this knowledge, Sieder-Tate correlation which does not contain any friction term [22] is used in the model. The correlation for three flow regimes is shown as

$$Nu_{lam} = 1.86\ (Re_{fluid}\ \mathrm{Pr})^{1/3} \left(\frac{\mu_{fluid}}{\mu_{film}}\right)^{0.14}, \tag{5.22}$$

$$Nu_{tran} = \left(1 - \frac{Re_{fluid} - Re_{lam}}{Re_{turb} - Re_{lam}}\right) Nu_{lam} + \left(\frac{Re_{fluid} - Re_{lam}}{Re_{turb} - Re_{lam}}\right) Nu_{turb}, \tag{5.23}$$

$$Nu_{turb} = 0.027\left(Re_{fluid}\right)^{0.8} Pr^{1/3} \left(\frac{\mu_{fluid}}{\mu_{film}}\right)^{0.14}, \tag{5.24}$$

where Nu is Nusselt number, Re is Reynolds Number, Pr is Prandtl number, μ_{fluid} is fluid dynamic viscosity calculated by flow temperature and μ_{film} is dynamic viscosity based on film temperature.

5.5.2. Contact Modeling

The current geometry has metal-to-metal contact which may prevent relative movement between two different components. In other words, the components can move independently as the geometry allows. The contact is named as two ways in the model: Weak Contact and Nearly Perfect Contact. These contacts refer that the engine confronts with what type of contact while operating.

Thermal modeling of these contacts is interpreted with contact resistance methodology, which is a well-known subject in heat transfer lecture, in 1D model, and these two also are determined by surface roughness, surface pressure and interfacial fluid

[23]. Conductivity is assumed 4000 W/mK for nearly perfect contact and 1000 W/mK for weak contact, and length and cross-section area are selected as unity.

Surface roughness in the contact regions is another issue that should be considered in terms of leakage. Surface roughness cannot be zero due to inadequacy of manufacturing technology in industry, and it is inevitable that flow can leak these regions. Accordingly, these locations are modeled with regard to flow as well as thermal effect.

As it is known to all, each component in the engine has tolerance which may come from manufacture and being assembled. When consider these effects, the gap in the model is taken as 0.25 mm for nearly perfect contact and 0.5 mm for weak contact.

The contact region HTC shall be attentively evaluated and defined since a flow can leak in there and convection term should be carefully entered as input. The current open literature does not contain such correlation for narrow gap, and hence a novel approach must be practiced. The contact gap is obviously small value together with hydraulic diameter is also small which means that Re is in laminar region for the model. Kays et al. [24] studied on a Nu for fully developed laminar flow in tubes of different cross section. If length is much higher than width, otherwise it goes to infinity, Nu for uniform surface temperature is 7.54. According to this knowledge, HTC for contact region is calculated for constant Nu. However, the FS does not include this correlation. A new Python script is coded for HTC correlation by using Customization Manager in the FS, named NGC. When the gap is given as input to the model, HTC is directly calculated for contact region.

5.5.3. Radiation Modeling

Radiation is a dominant factor for turbomachinery. Components, especially those interacting with main flow, have a very high temperature comparing to relatively low temperature components such as casing. This temperature difference affects radiative heating of the casing.

The geometry involves two concentric cylinders of same finite length (see Section 5.3.2). When imposing this geometric consideration to the radiation modeling, view factor is calculated based on book of Howel et al. [25]. The following equaiton shows that how view factor from hot part (1) to cold part (2) is calculated as

$$R = \frac{r_2}{r_1},$$

$$L = \frac{l}{r_1},$$

$$A = L^2 + R^2 - 1,$$

$$B = L^2 - R^2 + 1,$$

$$F_{2-1} = \frac{1}{R} - \frac{1}{\pi R}\left\{cos^{-1}\frac{B}{A} - \frac{1}{2L} * \left[\sqrt{(A+2)^2 - (2R)^2}cos^{-1}\frac{B}{RA} + Bsin^{-1}\frac{1}{R} - \frac{\pi A}{2}\right]\right\},$$

$$F_{1-2} = F_{2-1} * R, \tag{5.25}$$

$$F_{2-2} = 1 - \frac{1}{R} + \frac{2}{\pi R}tan^{-1}\frac{2\sqrt{R^2-1}}{L} - \frac{L}{2\pi R}\left[\frac{\sqrt{4R^2+L^2}}{L}sin^{-1}\frac{4(R^2-1)+\left(\frac{L^2}{R^2}\right)(R^2-2)}{L^2+4(R^2-1)} - sin^{-1}\frac{R^2-2}{R^2} + \frac{\pi}{2}\left(\frac{\sqrt{4R^2+L^2}}{L} - 1\right)\right],$$

where r_1 is radius of inner part, r_2 is radius of outer part, l is length of the duct, and F is view factor. Besides, radiation must be considered for outer surface of the engine because the outer surface sees ambient.

Emissivity in radiative heating is another parameter that affects heat flow. The emissivity value for nickel based alloys and high temperature, up to 850 K, is ranged between 0.65 and 0.95 [26,27,28]. Subsequently, this value is set to 0.7 which is a general practice. But also, it is not an unlikely assumption for the model.

5.5.4. Natural Convection Modeling

As mentioned in Chapter 4, still air approach for the engine outer casing is suitable for 1D modeling. The convective heating in this location is driven by buoyancy force. To calculate HTC, the correlation derived by Churchill and Chu [23,29] is used as

$$Nu = \left[0.60 + \frac{0.387 * Ra_D^{\frac{1}{6}}}{\left[1 + \left(\frac{0.559}{Pr} \right)^{\frac{9}{16}} \right]^{\frac{8}{27}}} \right]^2 \qquad Ra_D \leq 10^{12}, \tag{5.26}$$

where Nu is Nusselt number, Ra is Rayleigh number and Pr is Prandtl number.

The calculated HTC value is 9.75 W/m²K where Ra is 2.12E+9. However, the value that is obtained with above equation does not firmly represent HTC in the outer casing because the vibration of the engine and leakages at both bolts and contact locations affect HTC. Regarding this effect, HTC value is taken as 30 W/m²K.

6. RESULTS

Having discussed the modeling details in previous chapter, boundary condition and HTC value in the FS model, the test and the FS comparison, the sensitivity analysis results and geometric improvement will be presented in this chapter.

All temperature and pressure results are written as non-dimensional form. Both air and metal temperature are divided to T45 which is mass weighted average of total temperature at the 45 Station taken from CFD while mass weighted average of static pressure at the 45 Station, P45, taken from CFD is used for non-dimensional form of static pressure.

6.1. Boundary Condition Inputs

As explained in Section 5.4, the pressure and temperature boundary conditions are based on different sources like the test data and the CFD analysis. HTC for main flow path is another boundary condition for the FS, and it is calculated by using the Sieder-Tate correlation (see Section 5.5.1).

The BCs for the stations are tabulated in Table 6.1.

Table 6.1. Non-dimensional temperature and pressure boundary conditions values.

Station	**Non-Dimensional Total Temperature [K/K]]**	**Non-Dimensional Static Pressure [kPa/kPa]**
Inlet	0.573	2.403
45	1.010	2.170
46	1.010	1.830

Table 6.1. Non-dimensional temperature and pressure boundary conditions values (cont.).

Station	**Non-Dimensional Total Temperature [K/K]]**	**Non-Dimensional Static Pressure [kPa/kPa]**
46 Upper	0.941	1.731
47	0.925	1.349
47 Upper	0.937	1.428
48	0.925	1.041
48 Upper	0.865	1.008
Outlet	-	0.827
Inlet Upper Casing	0.566	-
Inlet Lower Casing	0.902	-
Outlet Casing	0.789	-
R1 Tip	0.942	-
R2 Tip	0.867	-

6.2. HTC Inputs

The geometry has an annular cross-section with finite length throughout main flow path (see Section 5.3.2). Sieder-Tate is initially suitable correlation since it is originally correlated for duct flow. To find the HTC value, geometric details of the annular cross-section, pressure, and temperature are the mandatory inputs to calculate Nusselt, Prandtl and Reynolds Numbers. Then, HTC is obtained.

Nevertheless, the main flow path is separated from the duct flow due to the presence of blades and rotation which affect the HTC value. The current correlation in the FS hence does not enough to represent HTC in the flow path. As a reason of this inadequacy, both

metal and air temperatures are assigned incorrectly. To put away this mismatch, the Sieder-Tate correlation requires additional coefficient. While finding the coefficient, fine tuning should be carried out until the temperature converges to the measured test value. As it will be seen following sections, the HTC values are rounded to the closest whole number.

In the geometry, there are some certain locations where HTC value is used as input and these are listed below:

- Through main flow path.
- 46 Upper.
- R1 Tip.
- 47 Upper.
- 48 Upper.
- R2 Tip.

The HTC value in main flow path, R1 Tip and R2 Tip is calculated based on Sieder-Tate correlation.

46 Upper, 47 Upper and 48 Upper have a different flow structure in comparison with interior of the casing since these three cavities are rotor stator cavity, and duct flow correlations in the literature or in the FS cannot properly represent to compute HTC value. Therefore, a HTC correlation which is different from Sieder-Tate is used. The Nu number in this correlation for Re_{rot} < 2.4*10^5 is written as

$$Nu = 0.616 * Pr^{1/3} * {Re_{rot}}^{0.5} = 0.616 * Pr^{\frac{1}{3}} * \left(\frac{\rho(\omega r)r}{\mu}\right)^{0.5}. \quad (6.1)$$

For Re_{rot} >3*10^5, the correlation becomes as

$$Nu = 0.0267 Pr^{2/3} {Re_{rot}}^{0.8}, \quad (6.2)$$

where Nu is Nusselt number, Pr is Prandtl number and Re_{rot} is rotational Reynolds number.

In this correlation, two different Nu is calculated. One is for rotor surface and the other is for rotor surface. To find these Nu numbers, Re_{rot} is the most dominant parameter. The Re_{rot} for rotor and stator surfaces is obtained as

$$\begin{aligned} Re_{rot} &= \frac{\rho(\omega r)r}{\mu} XK \qquad for\ stator\ surface, \\ Re_{rot} &= \frac{\rho(\omega r)r}{\mu}(1-XK) \qquad for\ rotor\ surface, \end{aligned} \tag{6.3}$$

where ρ is density, ω is angular velocity, r is radius, μ is dynamic viscosity and XK is swirl ratio.

The XK in Equation 6.3 is calculated based on 1D rotor-stator cavity balance [1]. While computing the XK, the difference between rotor and stator surface torques should be equal to angular momentum of the flow in the cavity. Sultanian [1] is formulated this balance as

$$\Gamma_{rotor} - \Gamma_{stator} = \sum_{j=1}^{n} \left(\dot{m}_j r_j^2 \omega_j XK\right)_{outlet} - \sum_{i=1}^{n} (\dot{m}_i r_i^2 \omega_i XK_i)_{inlet}, \tag{6.4}$$

rotor surface torque is written as

$$\Gamma_{rotor} = 0.044\rho(1-XK)^{1.35}\omega^2(r_2^5 - r_1^5)Re_{rot}^{-0.2}, \tag{6.5}$$

and stator surface torque is written as

$$\Gamma_{stator} = 0.066\rho XK^{1.87}\omega^2(r_2^5 - r_1^5)Re_{rot}^{-0.2}, \tag{6.6}$$

where Γ_{rotor} is rotor surface torque, Γ_{stator} is stator surface torque, $\dot{m}$ is mass flow rate, ω is angular velocity, r is radius, XK is swirl ratio, and i and j denote number of entering or leaving flow in the cavity while 1 and 2 designate inner and outer radius of surface.

To find XK value in that cavity, an iterative solution is carried out until the error between the surface torque and the angular momentum go to zero. When the iteration converges to zero, the outlet flow and cavity bulk XK will equal to computed value.

According to these locations, each cavity requires different additional coefficient to multiply with the calculated HTC value in accordance with proper correlation.

6.2.1. Main Flow Path

The obtained HTC value based on Sieder-Tate correlation for the main flow path is multiplied with 1.678. Assigning the coefficient, some iterative analyses were carried out, and the results converged to the test value. Eventually, the final value nearly becomes 650 W/m²K.

6.2.2. 46 Upper, 47 Upper and 48 Upper

46 Upper, 47 Upper and 48 Upper cavities are much more complicated region since the flow entrains in or leaves out the cavities locating on the right and the left of the rotor tip seals. The potential flow leakage in the geometry, Sector 2 and 4, are illustrated with red arrows in Figure 6.1.

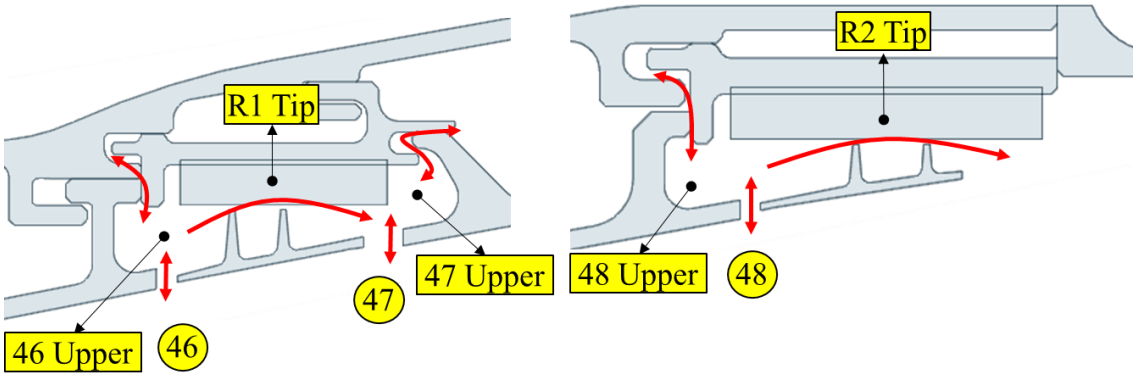

Figure 6.1. Possible flow leakage location in the rotor tips.

The coefficients at the cavities differ from each other due to the fact that the potential leakages from metal-to-metal contact or the main flow path disturb the flow in the voids. As a result, the coefficient which is calculated by using Equation 6.1 and 6.2 are shown in Table 6.2

Table 6.2. HTC values for the upper stations.

Station	**Coefficient**	**HTC [W/m²K]**
46 Upper	0.862	500
47 Upper	1.201	550
48 Upper	3.297	600

The table shows that the coefficients increase from 46 Upper to 48 Upper. In other word, the calculated HTC value in accordance with Equation 6.1 and 6.2 decreases from 46 Upper to 48 Upper. The coefficient and multiplied HTC value results are interpreted cavity-by-cavity.

For 46 Upper, rotation radius and XK in the cavities are the dominant parameter. Firstly, the rotation radius is taken as average radius of the cavity and this may not properly represent the radius of the sensor because the increase in the radius decreases the HTC, or vice versa. Secondly, the XK is computed based on average rotation radius and tangential velocity taken by CFD. In addition, this swirl ratio is a bulk swirl of the entire cavity. When considering the sensor location that is close to stator surface, this will cause the decrease in XK since stator surface tends to slow the flow, and hence Re_{rot} is affected. All in all, to capture metal surface temperature in this cavity the HTC value is multiplied with 0.862.

Same comments are valid for 47 Upper but it is seen that 47 Upper multiplied HTC value is higher than 46 Upper. The root cause is that the sensor location is in front of the local jet flow coming from Sector 3 internal cavity and filling to 47 Upper. This can increase the local HTC setting to 550 W/m²K.

As for 48 Upper, the Equation 6.1 or Equation 6.2 calculate small HTC value while the coefficient is out of concern. First of all, this cavity has lower mass flow rate comparing to the other two. This is one of the effects. Secondly, the temperature and pressure in this cavity is also lower which brings about the decrease in HTC value. Thirdly, same reasons in the 46 Upper and 47 Upper are also valid for 48 Upper. Eventually, 48 Upper HTC is higher than the rests. The dominant factor is as same as the 47 Upper. The cavity is directly interaction with the local jet flow coming from Sector 3 internal cavity.

6.2.3. R1 Tip and R2 Tip

The rotor tips have flow restrictive elements by creating pressure lose in order to minimize tip leakages. The restrictive elements in these regions tend to increase HTC because the rotor blades increase XK of the air. According to Sieder-Tate correlation, Table 6.3 shows both the coefficient and the HTC for the tips.

Table 6.3. HTC values for the tips.

Station	**Coefficient**	**HTC [W/m²K]**
R1 Tip	0.444	800
R2 Tip	0.259	500

The coefficients for the tips are less than 1. The reason is that Sieder-Tate correlation is originally used for duct flows but the tips have different structure to restrain the flow, and the FS does not contain any correlation for tip seal. This definitely hence affects calculated HTC value. The passed flow through the R1 Tip is higher than the R2 Tip, and Re is proportional to the mass flow. On the other side, Pr and dynamic viscosity for film and fluid decreases due to fact that the temperature at the R2 Tip is lower than R1 Tip. Hence, Nu at R1 tip is higher than R2 Tip. In order to capture metal temperature, the coefficients are iteratively calculated 0.444 and 0.259, respectively. This shows that Sieder-Tate correlation calculated higher HTC values that should require small coefficients.

6.3. Validation Through Comparison of FS and Test Results

The pressure and temperature boundary conditions (in Section 6.1) and the HTC values calculated for the main flow (in Section 6.2) are defined as input to the FS model and the result is obtained. The simulation was converged in 853 iterations and elapsed time was 575 seconds, nearly 8 minutes. The convergence criteria are set to 10^{-1} for mass balance and 10^{-5} for thermal heat balance.

In the following paragraphs, the results are compared sector-by-sector according to the corresponding location in the FS model of the sensor locations where the measurement result was taken in the test.

In the next figures which compare the test and the FS result, maximum and minimum value of the sensors are marked in these figures against to the FS result. The reason is that there are multiple sensors circumferentially surround the casing for the same axial location. In order to mitigate misunderstanding and to increase clarity of the result, the maximum and the minimum test values are tabulated for comparison. Additionally, standard deviation is accepted ±2σ for all measurement.

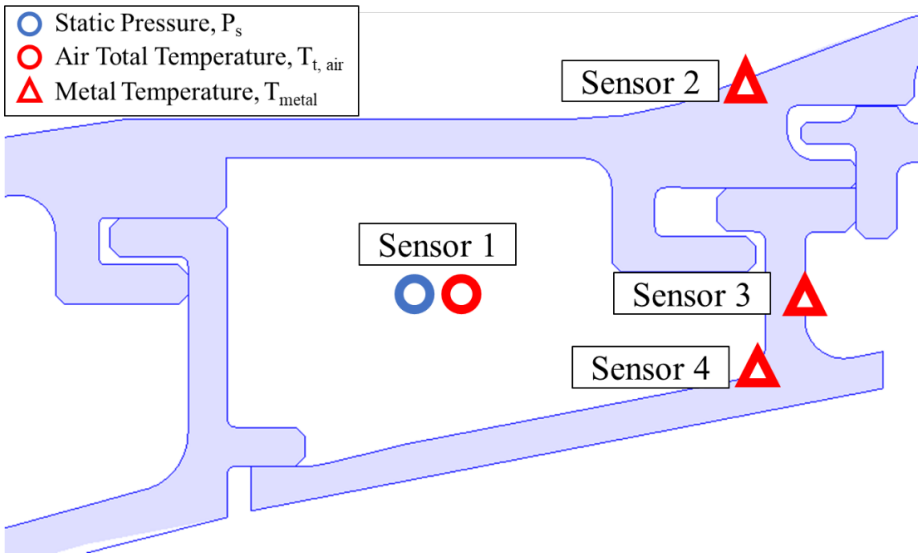

Figure 6.2. Sector 1 sensor locations.

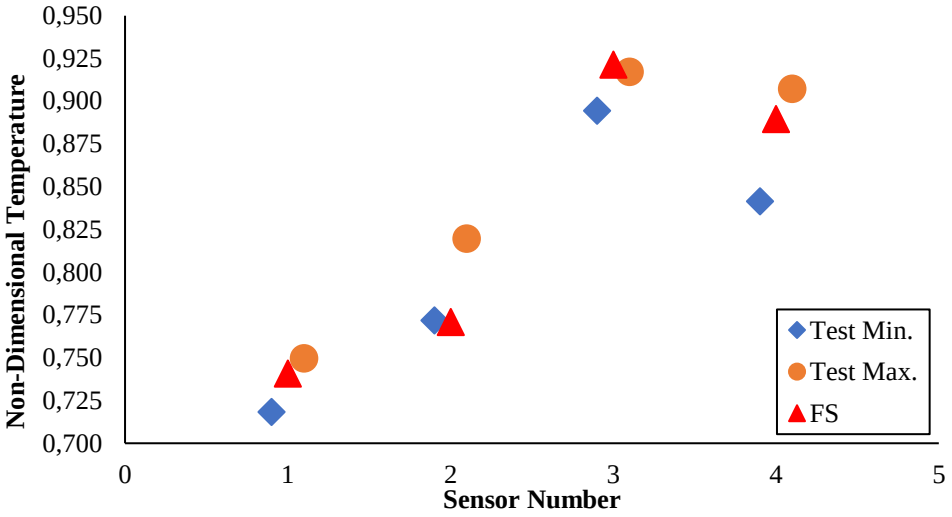

Figure 6.3. FS and the test temperature comparison at Sector 1.

Figure 6.3 shows the test and the FS comparison for the temperature sensors where their locations are marked in Figure 6.2. It is obviously seen that the 1D modeling results for Sensor 1 and 4 are between maximum and minimum value. Sensor 2 FS temperature is slightly less than minimum value; however, standard deviation for this sensor is about ±4 K and the FS result is in this range. Standard deviation is not non-dimensionalized because it will be too small and number of significant digits will be too many to show. When getting to Sensor 3, the FS is just above the maximum. Even though it is in range of standard deviation of the maximum value, the HTC in the main flow path, the temperature in the station, turbulence effect in the 46_Upper directly influence on thermal gradient.

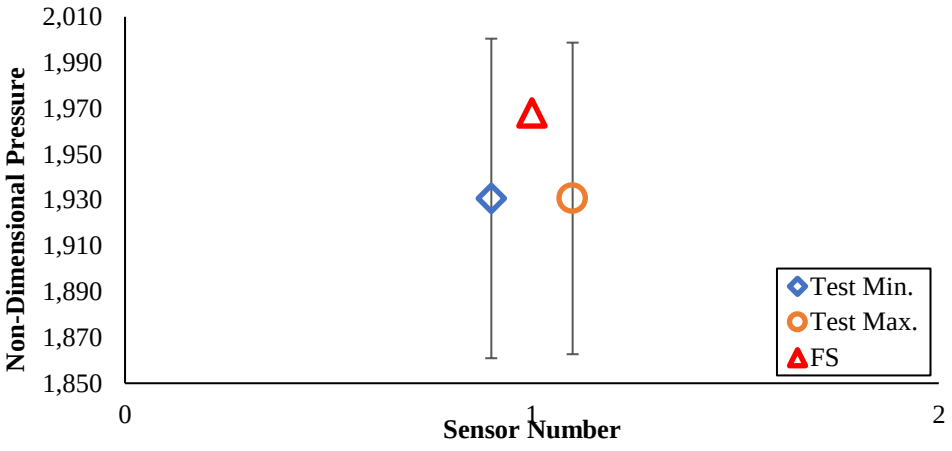

Figure 6.4. FS and the test static pressure comparison at Sector 1.

Figure 6.4 shows static pressure value at Sensor 1. It is seen that circumferential variation is not observed for the sensor in short, the maximum and the minimum values are same. The error bars in the figure depict standard deviation and the FS result is in this gap.

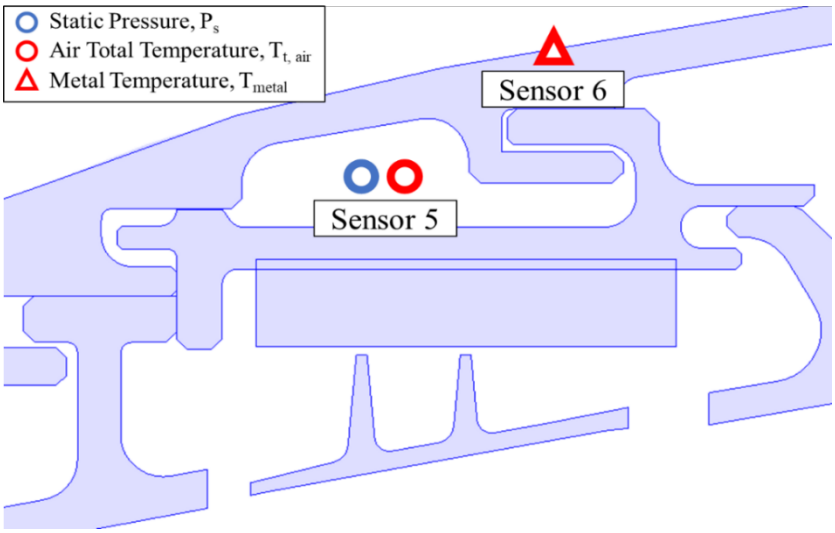

Figure 6.5. Sector 2 sensor locations.

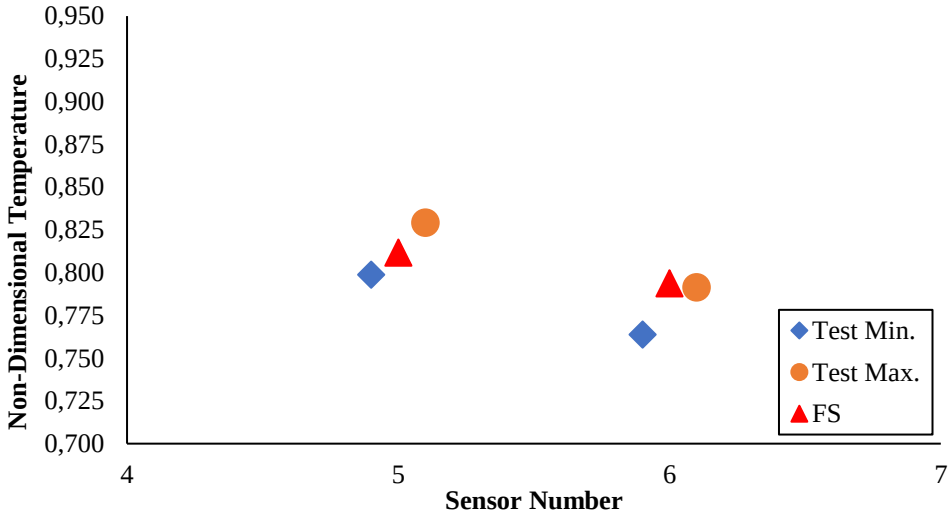

Figure 6.6. FS and the test temperature comparison at Sector 2.

Sector 2 measurement locations are illustrated in Figure 6.5. Sensor 5 FS temperature result is in the measured range of the test while FS results is slightly off comparing to the maximum at Sensor 6 (see Figure 6.6). This may occur that a heat source can increase local air temperature over the casing surface, and hence the metal temperature at that point can

exceed the test maximum value. However, it is also known that the FS is in standard deviation range that is ±2.8 K.

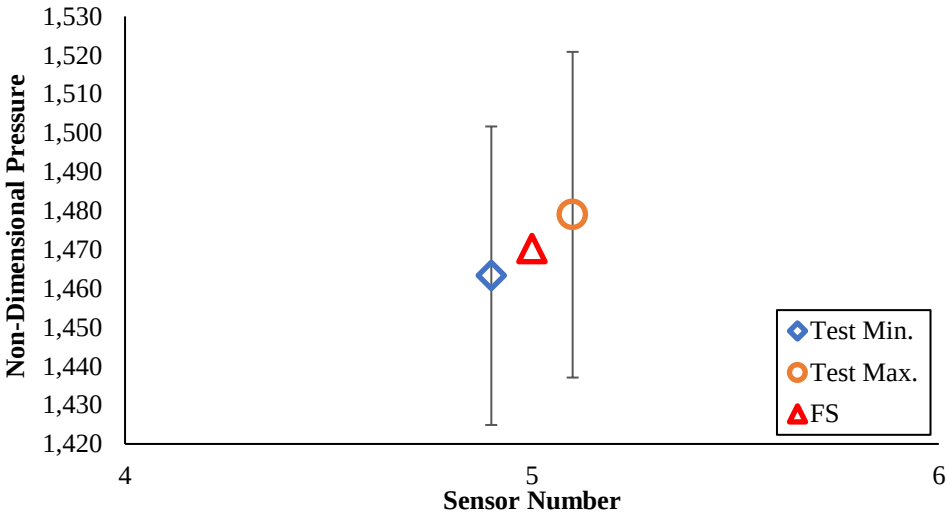

Figure 6.7. FS and the test static pressure comparison at Sector 2.

When coming to P_s at the Sensor 5, it is obviously seen that the FS precisely calculates the static pressure in Figure 6.7. This also implies that the engine geometry is properly imparted to the FS and the geometric inputs do not vary while working at the MTO condition.

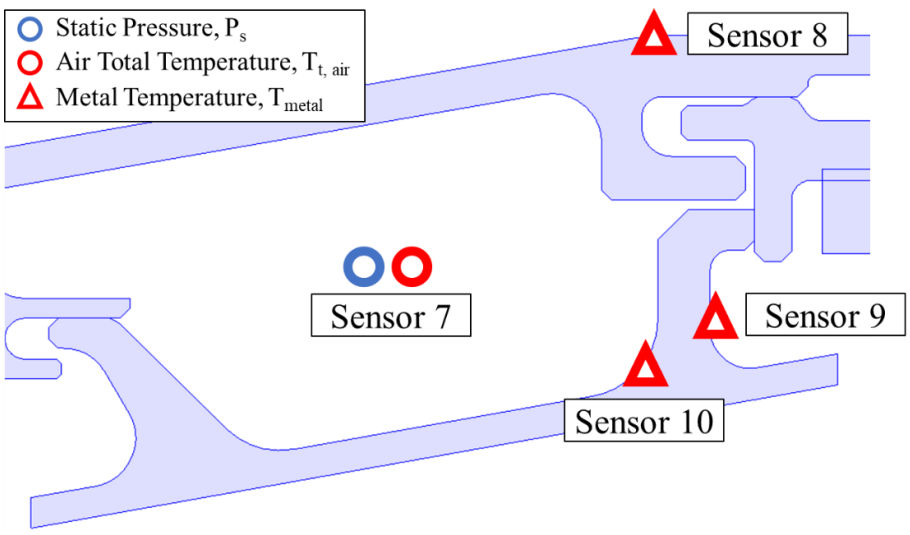

Figure 6.8. Sector 3 sensor locations.

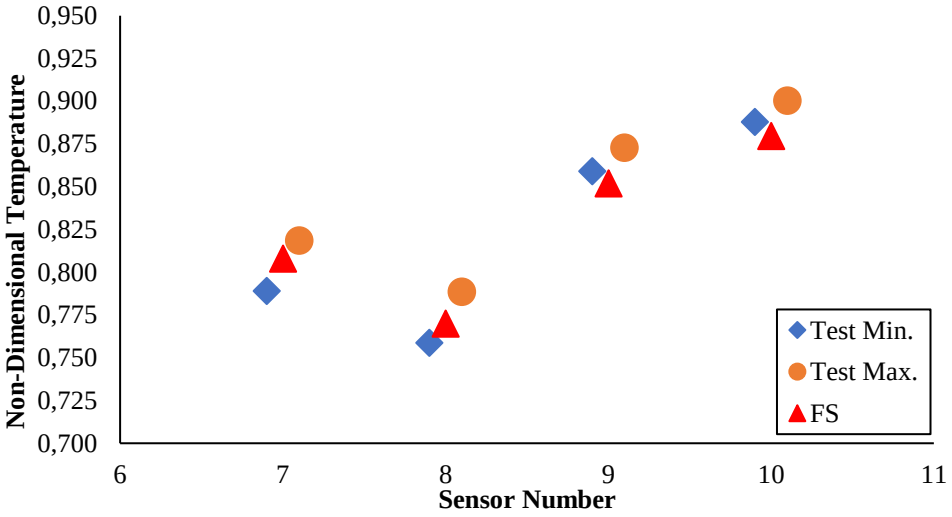

Figure 6.9. FS and the test temperature comparison at Sector 3.

The cavity locating above the Stator 2, called Sector 3, is illustrated that includes probe points in Figure 6.8. The Sensor 7 and 8 measuring air and metal temperature are between measurement ranges as shown in Figure 6.9. Rest of the two calculate the temperatures less than the minimums. But also, being emphasized that the differences between the FS and the minimum for Sensor 9 and 10 are below 1%. This small difference is fair enough for a 1D tool.

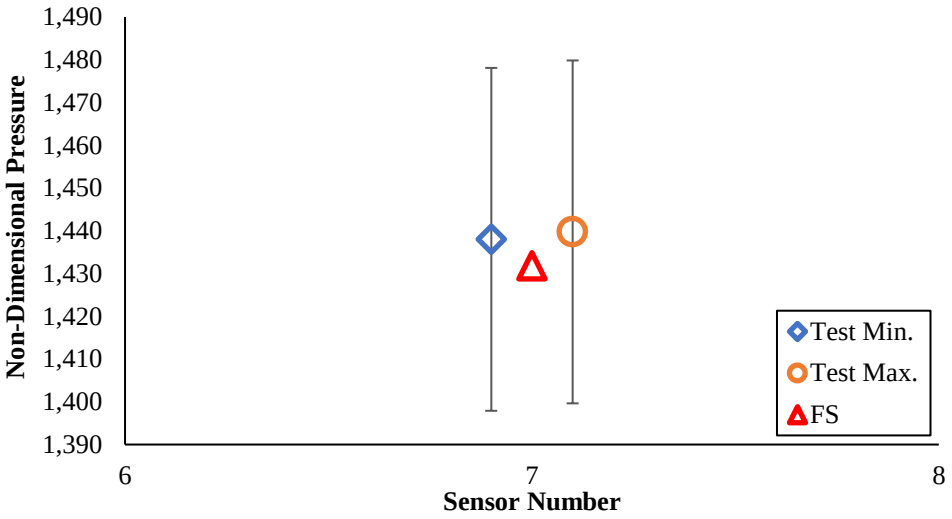

Figure 6.10. FS and the test static pressure comparison at Sector 3.

The air static pressure at the Sector 3 value is 1.432 whilst the test minimum value is 1.438 and the standard deviation is ±0.04, shown Figure 6.10. This shows that the FS properly calculates the P_s.

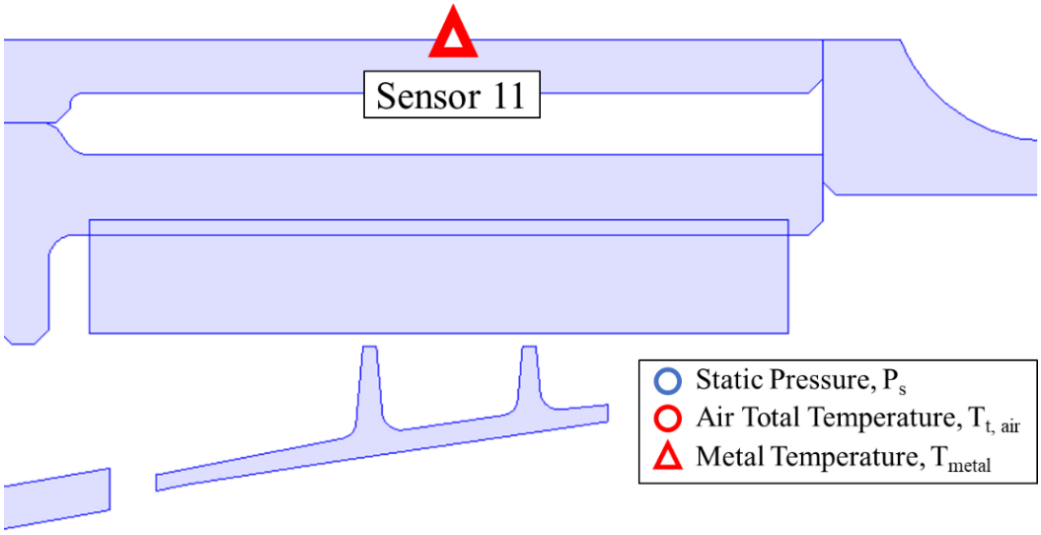

Figure 6.11. Sector 4 sensor location.

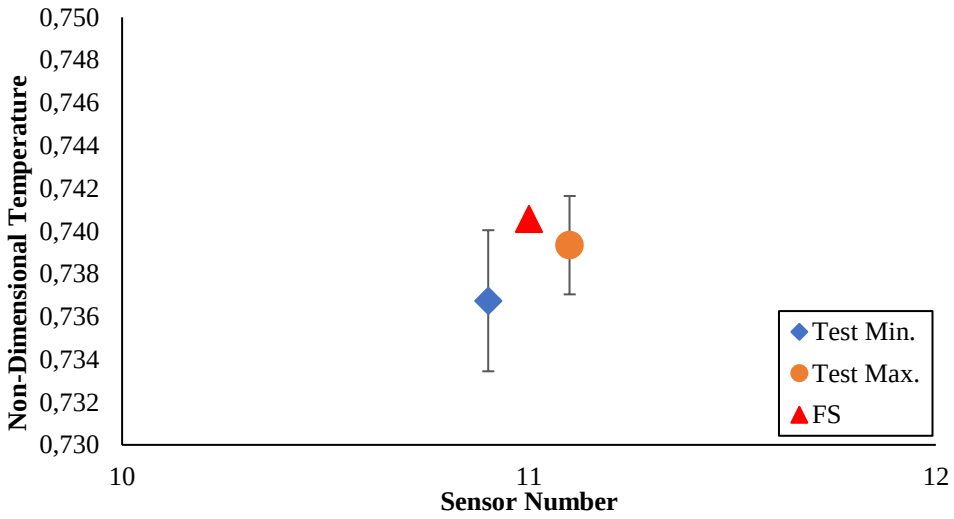

Figure 6.12. FS and the test temperature comparison at Sector 4.

At the last sector, there is just one metal temperature sensor placed on the casing outer surface, shown in Figure 6.11. The FS value is slightly higher than the maximum, nearly 0.0013 difference (see Figure 6.12). As it is seen that there is not any pressure

sensor in this cavity since the sector 4 is close the PT output and the pressure in this location tends to converge PT outlet tip pressure. It thus does not need to instrumentation.

All pressure and temperature results taken from the FS are in the minimum and the maximum. Although some FS results exceed the maximum or below the minimum, standard deviation comprises all the FS results.

There are multiple reasons why the FS measures the temperature and pressure less or high the range. The most prominent ones are that the probe can measure at wrong location after it is instrumented, the node number in the FS cannot be enough meaning that the components can be represented by more nodes to easily see temperature difference over a finite small axial or radial location, and external effects over the casing such as hot gas leakage through the ambient, bleed air and any heat source can affect temperature results. The FS model in the thesis does not cover the first and the last possible cause because these two come from the uncertainty of the test. The second cause relates to the modeling methodology of the FS. The node number can be increased to obviously see temperature gradient throughout any components. Yet, it should not be forgotten that this thesis aims to propose a 1D modeling strategy at preliminary design stage. Hence, the FS results is agreed well with the test results.

6.4. Sensitivity Analyses

Within the scope of the thesis, a set of sensitivity analysis is carried out in order to identify how the selected parameters affect the temperature and the pressure. Sensitivity analyses are divided into three:

- Natural Convection HTC effect
- Friction effect
- Another HTC correlation effect

While doing the analyses, all effects are studied as standalone model. In other words, cumulative effects are not considered. The main reason why the model is performed as standalone is to identify the pure response of the parameter on the model. Apart from them, boundary condition is not changed.

6.4.1. Natural Convection

PT casing outer surface is interaction with the ambient and still air approximation is assumed around engine mentioned in Section 5.5.4. However, it is also citied that the HTC is set to 30 W/m²K. To understand that how the created model is sensitive to HTC value of natural convection, the HTC is increased to 50 W/m²K and decreased to 10 W/m²K.

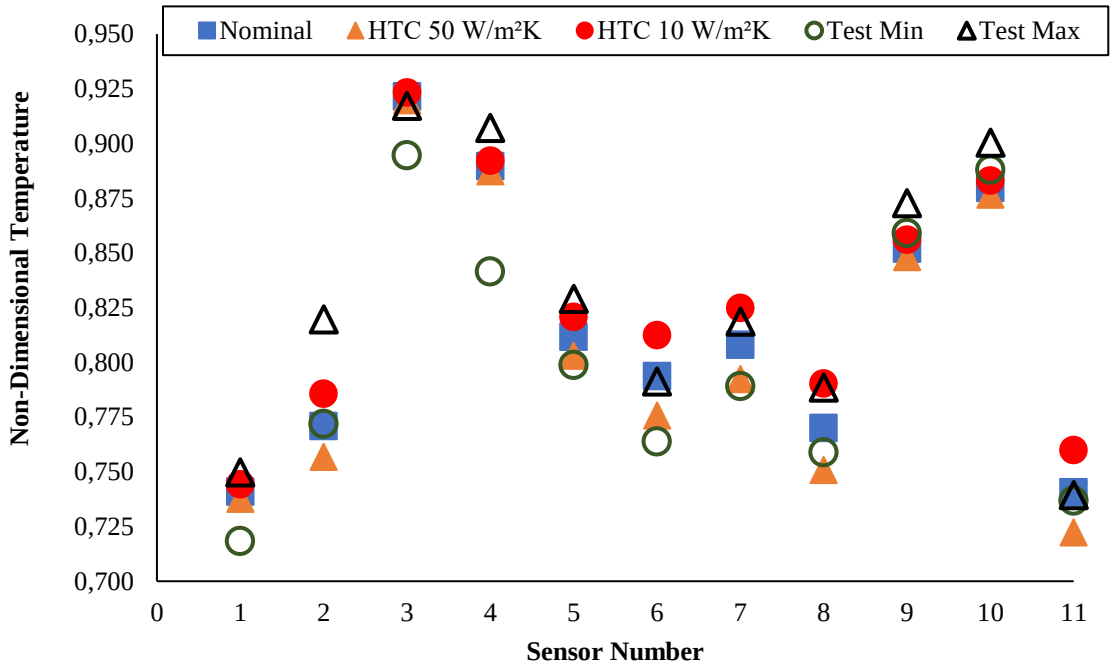

Figure 6.13. Temperature results of natural convection sensitivity analysis.

Figure 6.13 shows the temperature results for two HTC values against nominal conditions referring to the FS result compared with the test data. The main flow path temperature directly drives the Sensor 3, 4, 9, and 10 temperatures, and the results thus are not significantly varied for the two HTC values. Conversely, inner cavity air temperatures

(Sensors 1, 5, and 7) are influenced by HTC value. It is also seen that the difference between the measured air temperature values in the FS at these sensor locations increases toward the end of the module because the main flow path temperature decreases when reaching the module exit. Therefore, the main flow path dominancy on the module components goes down, and the natural convection effect is substantially noticed. When considering the metal temperatures placed on the casing's outer surface, Sensors 2, 6, 8, and 11 operate with the natural convection around the casing, and these four are the most affected sensors. Sensor 11 has the highest temperature difference since the cavity below the sensor possesses a small mass flow, and the HTC is lower than the other three. Therefore, natural convection significantly affects the metal temperature. The same interpretation is valid for Sensor 6 and 8; however, the differences for both are less than Sensor 11 because metal-to-metal contacts influence Sensor 6 and 8. As for Sensor 2, the metal temperature in Sector 1 is the dominant factor; hence, the natural convection effect in the sensor is lessened. In terms of pressure, the analysis results are not varied as expected. For three HTC values, the pressure sensors in the cavities vary around ±0.2 kPa.

Overall, when the sensitivity analysis results are compared with the test data for the Sensor 2, 6, 8 and 11, the analysis results are not in the test range for some sensors. Either the results are higher or lower than the test data. This comparison shows that the 30 W/m^2K input value is good enough to represent natural convection around the casing.

6.4.2. Friction

The model which is compared with the test data is frictionless meaning that pressure loss across the casing is not included the FS model. To understand how friction affects overall temperature distribution of the casing, a sensitivity analysis is performed. The friction in the flow region is assumed as 10 and 32 micrometers. For turbomachinery, surface roughness is a critic parameter, and 32 microns thus is too high to use in an engine. Yet, this roughness value is considered to see the effect on the casing model.

While calculating the friction factor in the FS, the well-known friction correlations in the literature for laminar and turbulent flows are used. For laminar flow, the fanning friction factor is calculated as

$$f = \frac{16}{Re}, \tag{6.4}$$

and the following equation, referenced from the Colebrook-White equation, is used for turbulent flow and it is expressed as [17]

$$f = 0.3313\left[ln\left(\frac{\varepsilon}{3.7D_h} + \frac{5.74}{Re^{0.9}}\right)\right]^{-2}. \tag{6.5}$$

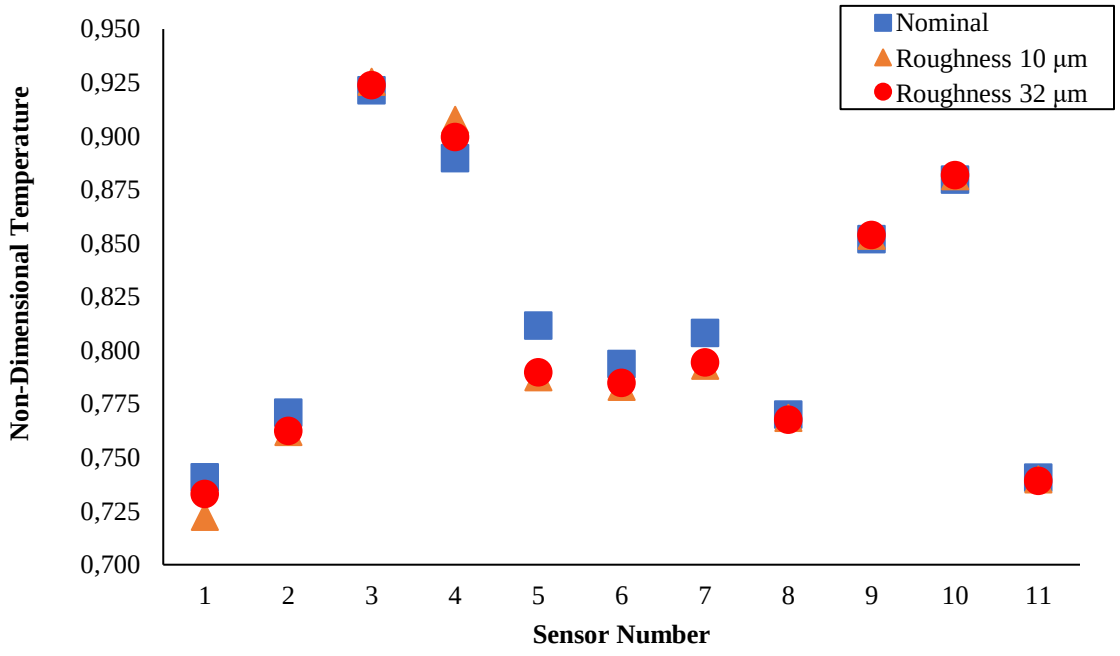

Figure 6.14. Temperature results friction effect sensitivity analysis.

Figure 6.14 presents the temperature value at the sensor location and the results is compared with the nominal FS model. Firstly, the air temperatures, Sensor 1, 5 and 7, in the sectors are evaluated. The 10 microns roughness for the first sensor analyzes lower temperature than the 32 microns since the P_s at downstream for the higher roughness value is lower than the fine one, and the pressure ratio goes up. Besides, pressure ratio between Station 46 and Sector 1 inner pressure is also increases when roughness is set to 32 microns. Thus, the main flow leakage at the contact location heats the inner cavity more

than the 10 microns and the Sector 1 air temperature rises up even if the 10 microns is lower than the nominal. Due to the fact that the air temperature is linked to each other, same trend is observed for the Sensor 5 and 7. When evaluating the casing outer surface metal temperatures (Sensor 2, 6, 8 and 11), these sensors follow same pattern with respect to the air temperatures. However, the last two sensors nearly measure same metal temperature values. The reason is that Sector 3 ending and Sector 4 indeed work in small pressure ratio, and hence the metal temperatures do not show obvious variation while changing the roughness. The Sensor 3 and 9 are directly interacting with the boundary conditions, and thus the temperatures show minor change, just ±1K. The Sensor 4 temperature value is opposite to the Sensor 1 trend, and if sorting the HTC values in the Sector 1 from largest to smallest, the order is Nominal, 32 microns and 10 microns. Seeing that the lowest HTC possesses the highest temperature since the convective resistance is low and the temperature is high. The remaining sensor number is 10 which has same with the Sensor 8 and 11 interpretations to explain temperature.

6.4.3. HTC Correlation Effect

The last sensitivity analysis comprises of HTC correlation effect on the 1D model. As explained in Section 5.5.1, the FS has proper HTC correlation to simulate any model but there are just two correlations to use in this study which are Sieder-Tate and Gnielinski. The former is the base correlation that is used in the nominal model and the latest one is the only correlation that can be utilized for sensitivity analysis.

The main difference between Gnielinski and Sieder-Tate (see Equation 5.22-24) is friction term in turbulent flow and laminar flow Nusselt number calculation. Gnielinski correlation for three flow regimes is expressed as

$$Nu_{lam} = \frac{0.688\, Re_{fluid} \dfrac{Pr * D_h}{L}}{1 + 0.04 \left(Re_{fluid} \dfrac{Pr * D_h}{L} \right)^{2/3}}, \tag{6.6}$$

$$Nu_{tran} = \left(1 - \frac{Re_{fluid} - Re_{lam}}{Re_{turb} - Re_{lam}}\right) Nu_{lam} + \left(\frac{Re_{fluid} - Re_{lam}}{Re_{turb} - Re_{lam}}\right) Nu_{turb}, \quad (6.7)$$

$$Nu_{turb} = \frac{(Re_{fluid} - 1000)0.5Prf}{1 + 12.7\sqrt{0.5f}(Pr^{2/3} - 1)}, \quad (6.8)$$

where D_h is hydraulic diameter, L is length of the pipe and f is Fanning friction factor.

The Sieder-Tate correlation in the 10 microns FS models in the previous sensitivity study is replaced by Gnielinski. This is because, as explained, friction is included in this correlation and the HTC value is calculated. Afterwards, the results are compared with the Nominal model.

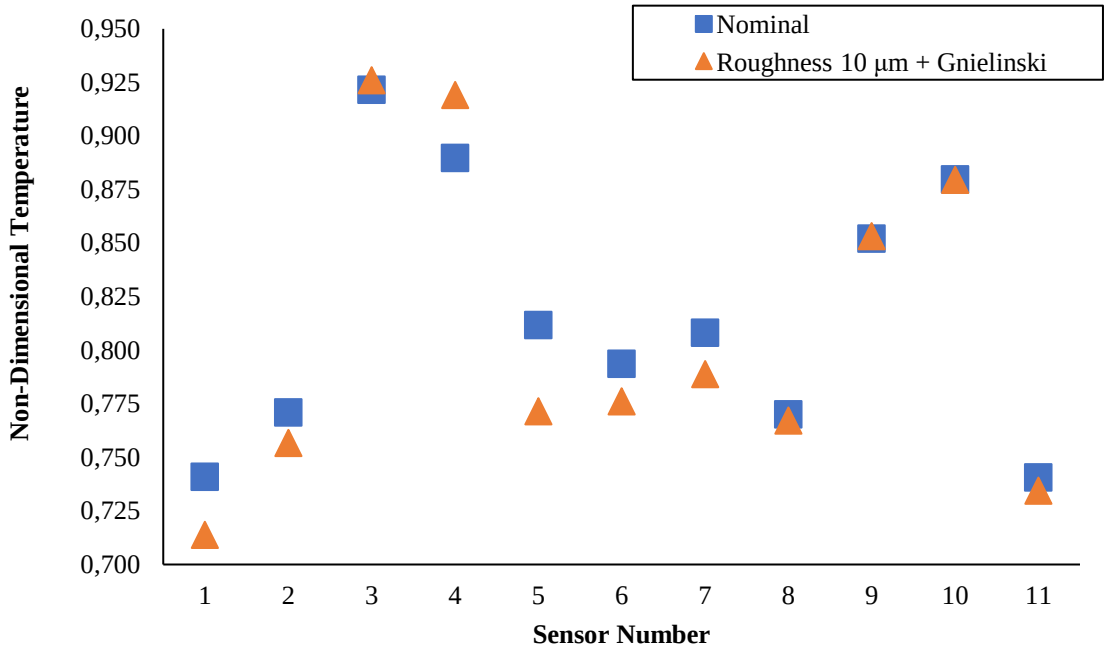

Figure 6.15. Temperature results of HTC sensitivity analysis.

Figure 6.15 shows the Gnielinski correlation effect on the temperature sensors in the casing. The first insight, the temperatures demonstrate similar trend in contrast with 10 microns roughness model in the sensitivity analysis. Calculated HTC value in Gnielinski correlation is less than the Sieder-Tate due to the difference between two correlations, and

the temperatures declines. Moreover, when the Gnielinski is compared with the test result, the Sieder-Tate conveniently calculates the HTC again.

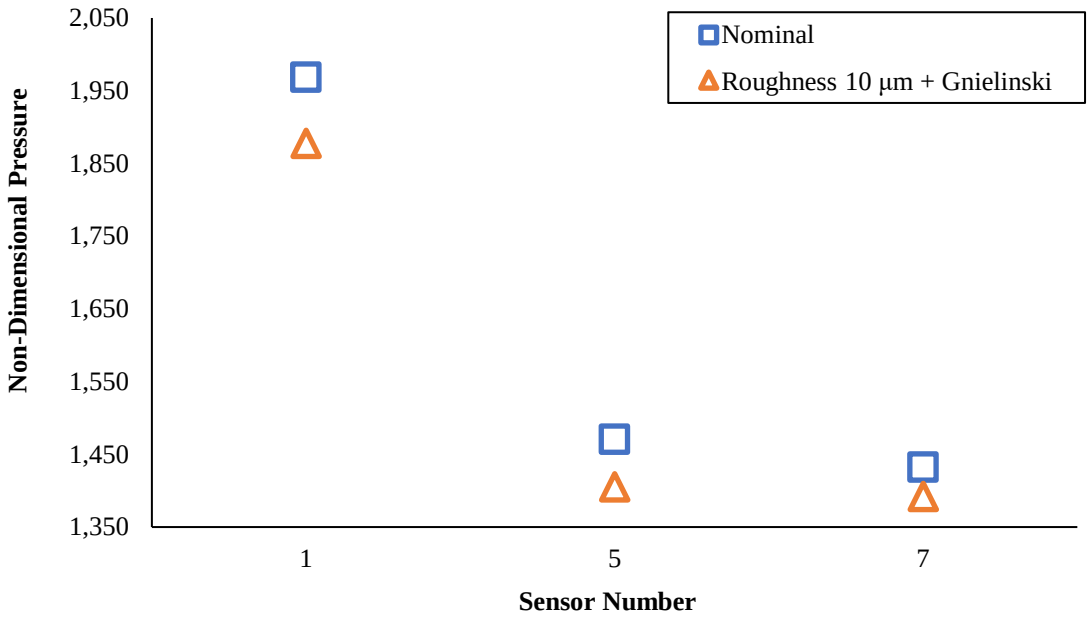

Figure 6.16. Pressure results of HTC sensitivity analysis.

The HTC sensitivity analysis is compared in terms of pressure at the Sensor 1, 5 and 7, shown in Figure 6.16. As expected, the pressure moderately goes down since the friction increases the pressure losses along the path. Hence, the pressure result at nominal model that is frictionless is higher than the other model.

All in all, the Figure 6.15 and Figure 6.16 state that Sieder-Tate correlation is well enough to model any casing geometry.

6.5. Geometric Improvement

When the FS analysis result is investigated, the metal temperature at the R1 Shroud looks high enough, or close to the metal service temperature. This high temperature tends to increase thermal expansion of the shroud, and finally the rotor tip clearance gets large.

This increment at the rotor tip clearance can decrease overall efficiency of the PT module. In order to enhance both the efficiency and to narrow the clearance, a new geometry is proposed to mitigate thermal expansion and prevent pushing of R1 Shroud from S1.

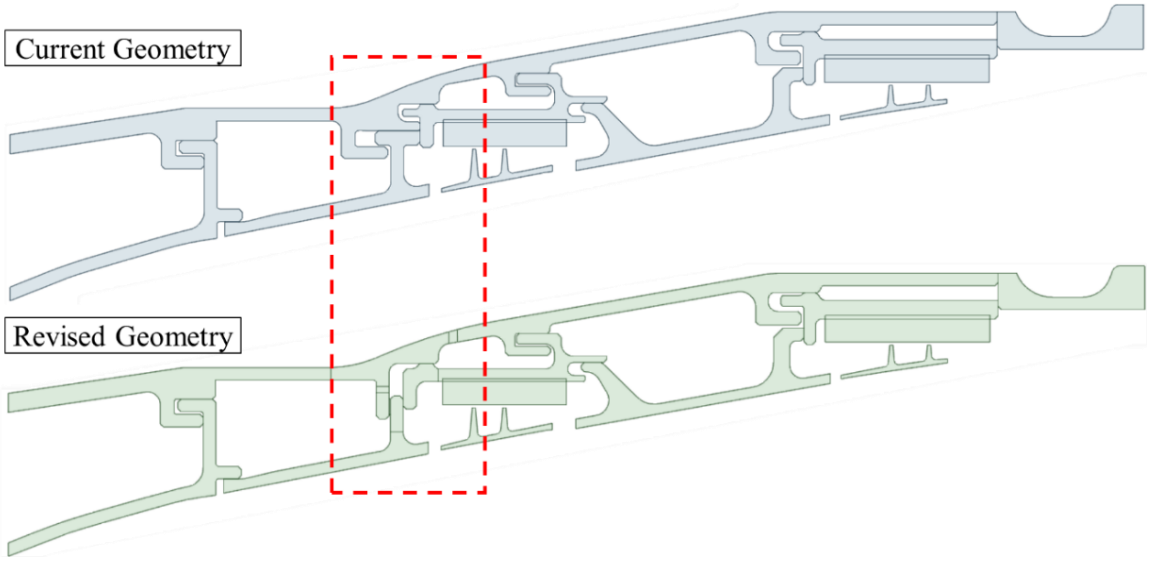

Figure 6.17. Difference between the current and the revised geometries.

Figure 6.17 shows the difference between the current and the revised geometries, marked in red dotted rectangle. The new geometry includes two impingement holes; first hole is located axial direction and the upstream pressure is Sector 1 cavity, and second hole has radially inward flow coming from compressor with higher pressure and lower temperature. Beside two impingement holes, contact surfaces between components are minimized which decrease conductive heat transfer. The last revision is that radial movement capability is also gained to the S1. This provides that thermal expansion of the S1 does not push to R1 shroud and the clearance does not change.

When comparing the metal temperature of the components, the revised model provides approximately 70 K bulk temperature decrease on R1 Shroud. It is interpreted that this fall decreases rotor tip clearance comparing to the current one and PT efficiency.

7. CONCLUSION

A 1D thermo-fluid network of a power turbine casing at a preliminary design stage was modelled in this study by using flow and thermal network elements in the model. First of all, the flow network was created and then thermal network was implemented on the flow network. While establishing the model, a commercial 1D network solver, called Flow Simulator, was used to carry out the modeling.

A test campaign that was instrumented a large number of static pressure, metal temperature and total temperature sensors to understand thermal and flow characteristic of the engine was carried out at maximum take-off condition in an altitude where the campaign was mounted.

Proposed 1D coupled network modeling methodology in the FS was well defined to simulate PT casing which has annular cross-section since the users can easily define geometric properties on the model. Moreover, the methodology contains the corner points to create any 1D model at preliminary design stage such that heat transfer coefficient selection, contact, radiation and natural convection modeling.

The boundary conditions that were entered in the model were fed from different sources. Due to lack of sensor at certain locations, CFD results were directly used as boundary condition in the FS. Additionally, a scaling methodology was carried out because CFD and the test results for three locations in the model that are R1 tip, R2 tip and 47 Upper did not possess any data.

Some essential outcomes for this study which were emphasized in Chapter 6 are listed below:

- The air and metal temperatures, and static pressures results in 1D model are well captured with the test results.

- Heat transfer coefficient multipliers across main flow path are properly defined to represent the temperatures along the casing.
- Natural convection heat transfer coefficient which is set to 30 W/m²K is a good approach to represent other effects like vibration and leakages around the casing.
- The friction in the model measures lower temperature and pressure value than frictionless model. Therefore, frictionless model is not a far approach for casing modeling. Another reason why frictionless model is more suitable than frictional model is that while the FS model is being constructed, 0.25 and 0.5 mm contact definitions (see Section 5.5.2) obliquely include friction term.
- Sieder-Tate correlation shows better values when comparing to Gnielinski correlation.
- Proper cooling system is used to control both metal temperature and rotor tip clearances.

This 1D thermo-fluid network model can be used for future studies to model the other engine modules at preliminary design stage so that the computational time and labor force may be lessen. Furthermore, the HTC value which is obtained by using additional coefficient can be extensively carried out to find appropriate correlation which reflects flow characteristic more conveniently. Finally, 1D model can be easily manipulated to optimize cooling system in terms of metal temperature and internal pressure in order to find out well designed module geometry.

According to this consequence, a proper heat transfer coefficient correlation might be considered for further studies to take away constant coefficient, and instead a comprehensive correlation can be derived. Besides, the current geometry can be revised to decrease metal and air temperatures. Hence, the tip leakages and the conduction path between components might be minimized.

REFERENCES

1. Sultanian, B. K., *Gas Turbines: Internal Flow Systems Modeling*, Cambridge University Press, New York, 2018.

2. Thorpe, S. J., R. J. Miller, S. Yoshino, R. W. Ainsworth and N. W Harvey, “The Effect of Work Processes on The Casing Heat Transfer of a Transonic Turbine”, *Journal of Turbomachinery*, Vol. 129, No. 1, pp. 84–91, 2007.

3. Dann, A., P. Dhopade, M. Bacic, P. Ireland and L. Lewis, “Experimental and Numerical Investigation of Annular Casing Impingement Arrays for Faster Casing Response”, *Journal of Engineering for Gas Turbines and Power*, Vol. 139, No. 9, p. 092603, 2017.

4. Dann, A. G., S. J. Thorpe, L. Lewis, and P. Ireland, "Innovative Measurement Techniques for a Cooled Turbine Casing Operating at Engine Representative Thermal Conditions", paper presented at the *Proceedings of the ASME Turbo Expo 2014: Turbine Technical Conference and Exposition*, Dusseldorf, Germany, 2014.

5. Wang, W., H. Zhang, P. Liu, Z. Li, W. Ni, H. Uechi and T. Matsumura, “A Finite Element Method Approach to the Temperature Distribution in the Inner Casing of a Steam Turbine in a Combined Cycle Power Plant”, *Applied Thermal Engineering*, Vol. 105, pp. 18–27, 2016.

6. Pilkington, A., B. Rosic and S. Horie, “Methods for Controlling Gas Turbine Casing Flows During Engine Shutdown”, *Mathematics Teaching-Research Journal*, Vol. 4, No. 4, pp. 103–118, 2011.

7. Muller, Y., "Integrated Fluid Network-Thermomechanical Approach for the Coupled Analysis of a Jet Engine", paper presented at the *Proceedings of the ASME Turbo Expo 2009: Power for Land, Sea, and Air*, Florida, USA, 2009.

8. Tondello, G, W. Boruszewski, F. Mengele, M. Assato, S. Shimizu, and S. Ziegler, "Coupled Simulation of the Secondary Air Flow, Heat Transfer, and Structural

Deflection of a Gas Turbine Engine", paper presented at the *Proceedings of the ASME Turbo Expo 2012: Turbine Technical Conference and Exposition*, Copenhagen, Denmark, 2012.

9. Caty, F., 2012, *Design of Secondary Air System and Thermal Models for Triple Spool Jet Engines*, M.S. Thesis, Kungliga Tekniska Högskolan Industrial Engineering and Management.

10. Alizadeh, M., A. Izadi, A. Fathi and H. Khaledi, “Flow and Heat Transfer Analysis of Turbine Blade Cooling Passages Using Network Method”, paper presented at the *Proceedings of the ASME 2012 Gas Turbine India Conference*, Maharashtra, India, 2012.

11. Ganine, V., N. Hills, M. Miller, C. Barnes, S. Curzons, L. Turner and P. Smout, "Implicit Heterogeneous 1D/2D Coupling for Aero-Thermo-Mechanical Simulation of Secondary Air Systems", paper presented at the *Proceedings of the ASME Turbo Expo 2015: Turbine Technical Conference and Exposition*, Montreal, Canada, 2015.

12. Ba, W. and X. Ren, "Aero-Thermal Coupled Throughflow Method with Cooling Model Based on Flow Network Analysis" paper presented at the *Proceedings of the ASME Turbo Expo 2017: Turbomachinery Technical Conference and Exposition*, North Carolina, USA, 2017.

13. Collins, M., K. Chana and T. Povey, “Application of Film Cooling to an Unshrouded High-Pressure Turbine Casing”, *Journal of Turbomachinery*, Vol. 139, No. 6, p. 061010, 2017.

14. Jalali, R., M. Darbandi and G. E. Schneider, “Robust 1-D Fluid Flow and Heat Transfer Predictions in Gas Turbine Cooling Passages”, *AIAA Propulsion and Energy Forum and Exposition*, 2019.

15. Hunt, D., Y. Yuan and I. Gardner, "Modelling Conjugate Heat Transfer within a Gas Turbine Secondary Air System Using 1D and 2-3D Solid Models in Thermo-Fluid System Simulation", presented at the *Proceedings of the ASME Turbo Expo 2021: Turbomachinery Technical Conference and Exposition*, Virtual, Online, 2021.

16. Uyav, O., A. C. Arikan, M. Kocagul, A. Ertas, J. Bruns and A. Jayanthi, “Gas Turbine Secondary Air Systems Modeling”, presented at the *Proceedings of the ASME Turbo Expo 2022: Turbine Technical Conference and Exposition*, Rotterdam, Netherland, 2022.

17. Altair Flow Simulator 2022 User Manual, Altair Inc., Troy, NY, 2022.

18. Blevins, R. D., *Applied Fluid Dynamics Handbook*, Krieger Publishing Company, New York, 2003.

19. Muzychka, Y. S. and M. M. Yovanovich, “Laminar Forced Convection Heat Transfer in the Combined Entry Region of Non-Circular Ducts”, *Journal of Heat Transfer*, Vol. 126, No. 1, pp. 54–61, 2004.

20. Gnielinski, V., “New Equations for Heat and Mass Transfer in The Turbulent Flow in Pipes and Channels”, *International Chemical Engineering*, Vol.16, pp. 359-368, 1976.

21. Kakac, S., R. K. Shah and W. Aung, *Handbook of Single-Phase Convective Heat Transfer*, John Wiley and Sons Inc., New York, 1987.

22. Sieder, E. N. and G. E. Tate, “Heat Transfer and Pressure Drop of Liquids in Tubes”, *Industrial & Engineering Chemistry*, Vol. 28, No. 12, pp. 1429–1435, 1936.

23. Incropera, F. P., T. L. Bergman and A. Lavine, *Fundamentals of Heat and Mass Transfer*, Eight Edition, Wiley, New York, 2017.

24. Kays, W., M. Crawford and B. Weigand, *Convective Heat and Mass Transfer*, Fourth Edition, McGraw-Hill Series in Mechanical Engineering, New York, 2005.

25. Howell, J. R., M. P. Mengüç, K. Daun and R. Siegel, *Thermal Radiation Heat Transfer*, Seventh Edition, CRC Press, Florida, 2020.

26. Skubisz, P. and P. Micek, “Determination of Emissivity Characteristics for Controlled Cooling of Nickel-Alloy Forging”, *Solid State Phenomena*, Vol. 208, pp. 1–7, 2014.

27. Keller, B. P., S. E. Nelson, K. L. Walton, T. K. Ghosh, R. V. Tompson, and S. K. Loyalka, “Total Hemispherical Emissivity of Inconel 718”, *Nuclear Engineering and Design*, Vol. 287, pp. 11–18, 2015.

28. Greene, G. A., “Dependence of Total Hemispherical Emissivity of Inconel-718 on Surface Oxidation and Temperature”, *USDOE Office of Energy Research*, 1999.

29. Churchill, S. W. and H. H. S. Chu, “Correlating Equations for Laminar and Turbulent Free Convection from A Vertical Plate”, *International Journal of Heat and Mass Transfer*, Vol. 18, No. 11, pp. 1323–1329, 1975.